



MagMaR III—Resisting the Pressure, Is the Magnetic Field Overwhelmed in NGC6334I?

Paulo C. Cortés^{1,2}, Josep M. Girart^{3,4}, Patricio Sanhueza^{5,6}, Junhao Liu⁵, Sergio Martín^{1,7}, Ian W. Stephens⁸, Henrik Beuther⁹, Patrick M. Koch¹⁰, M. Fernández-López¹¹, Álvaro Sánchez-Monge^{12,13}, Jia-Wei Wang¹⁴, Kaho Morii^{15,16}, Shanghuo Li⁹, Piyali Saha¹⁶, Qizhou Zhang¹⁷, David Rebolledo^{1,2}, Luis A. Zapata¹⁸, Ji-hyun Kang¹⁹, Wenyu Jiao^{20,21}, Jongsoo Kim¹⁹, Yu Cheng⁵, Jihye Hwang¹⁹, Eun Jung Chung¹⁹, Spandan Choudhury¹⁹, A-Ran Lyo¹⁹, and Fernando Olguin²²

¹ Joint ALMA Observatory, Alonso de Córdova 3107, Vitacura, Santiago, Chile; paulo.cortes@alma.cl

² National Radio Astronomy Observatory, 520 Edgemont Road, Charlottesville, VA 22903, USA

³ Institut de Ciències de l'Espai (ICE-CSIC), Campus UAB, Carrer de Can Magrans S/N, E-08193 Cerdanyola del Vallés, Catalonia, Spain

⁴ Institut d'Estudis Espacials de Catalunya (IEEC), E-08034 Barcelona, Catalonia, Spain

⁵ National Astronomical Observatory of Japan, 2-21-1 Osawa, Mitaka, Tokyo 181-8588, Japan

⁶ Department of Astronomical Science, SOKENDAI (The Graduate University for Advanced Studies), 2-21-1 Osawa, Mitaka, Tokyo 181-8588, Japan

⁷ European Southern Observatory, Alonso de Córdova 3107, Vitacura, Santiago, Chile

⁸ Department of Earth, Environment and Physics, Worcester State University, Worcester, MA 01602, USA

⁹ Max Planck Institute for Astronomy, Königstuhl 17, 69117 Heidelberg, Germany

¹⁰ Institute of Astronomy and Astrophysics, Academia Sinica, 11F of Astronomy-Mathematics Building, AS/NTU No.1, Sec. 4, Roosevelt Road, Taipei 10617, Taiwan, People's Republic of China

¹¹ Instituto Argentino de Radioastronomía (CCT-La Plata, CONICET; CICIPBA; UNLP), C.C. No. 5, 1894, Villa Elisa, Buenos Aires, Argentina

¹² Institut de Ciències de l'Espai (ICE, CSIC), Carrer de Can Magrans s/n, E-08193, Bellaterra, Barcelona, Spain

¹³ Institut d'Estudis Espacials de Catalunya (IEEC), E-08034, Barcelona, Spain

¹⁴ Academia Sinica Institute of Astronomy and Astrophysics, No.1, Sec. 4., Roosevelt Road, Taipei 10617, Taiwan

¹⁵ Department of Astronomy, Graduate School of Science, The University of Tokyo, 7-3-1 Hongo, Bunkyo-ku, Tokyo 113-0033, Japan

¹⁶ National Astronomical Observatory of Japan, National Institutes of Natural Sciences, 2-21-1 Osawa, Mitaka, Tokyo 181-8588, Japan

¹⁷ Harvard-Smithsonian Center for Astrophysics, 60 Garden Street, Cambridge, MA 02138, USA

¹⁸ Instituto de Radioastronomía y Astrofísica, Universidad Nacional Autónoma de México, P.O. Box 3-72, 58090, Morelia, Michoacán, Mexico

¹⁹ Korea Astronomy and Space Science Institute (KASI), 776 Daedeokdae-ro, Yuseong-gu, Daejeon 34055, Republic of Korea

²⁰ Kavli Institute for Astronomy and Astrophysics, Peking University, Haidian District, Beijing 100871, People's Republic of China

²¹ Department of Astronomy, School of Physics, Peking University, Beijing 100871, People's Republic of China

²² Institute of Astronomy and Department of Physics, National Tsing Hua University, Hsinchu 30013, Taiwan

Received 2024 March 14; revised 2024 May 28; accepted 2024 June 17; published 2024 August 28

Abstract

We report on Atacama Large Millimeter/submillimeter Array observations of polarized dust emission at 1.2 mm from NGC6334I, a source known for its significant flux outbursts. Between five months, our data show no substantial change in total intensity and a modest 8% variation in linear polarization, suggesting a phase of stability or the conclusion of the outburst. The magnetic field, inferred from this polarized emission, displays a predominantly radial pattern from northwest to southeast with intricate disturbances across major cores, hinting at spiral structures. Energy analysis of CS ($J = 5 \rightarrow 4$) emission yields an outflow energy of approximately 3.5×10^{45} erg, aligning with previous interferometric studies. Utilizing the Davis–Chandrasekhar–Fermi method, we determined magnetic field strengths ranging from 1 to 11 mG, averaging at 1.9 mG. This average increases to 4 ± 1 mG when incorporating Zeeman measurements. Comparative analyses using gravitational, thermal, and kinetic energy maps reveal that magnetic energy is significantly weaker, possibly explaining the observed field morphology. We also find that the energy in the outflows and the expanding cometary HII region is also larger than the magnetic energy, suggesting that protostellar feedback may be the dominant driver behind the injection of turbulence in NGC6334I at the scales sampled by our data. The gas in NGC6334I predominantly exhibits supersonic and trans-Alfvénic conditions, transitioning towards a super-Alfvénic regime, underscoring a diminished influence of the magnetic field with increasing gas density. These observations are in agreement with prior polarization studies at 220 GHz, enriching our understanding of the dynamic processes in high-mass star-forming regions.

Unified Astronomy Thesaurus concepts: [Interstellar magnetic fields \(845\)](#); [Star Formation \(1569\)](#); [Molecular Gas \(1073\)](#)

1. Introduction

Stars are formed within dense and weakly ionized gas and dust complexes commonly known as molecular clouds, where the current paradigm suggests that they are filamentary in

nature (Arzoumanian et al. 2011). Despite their weak ionization rates, magnetic fields thread these regions and are unavoidable. In the past decades, the advent of millimeter and submillimeter interferometers such as the Berkeley, Illinois, and Maryland Association, the Combined Array for Research in Millimeter-wave Astronomy, and the Sub-Millimeter Array (SMA) began to allow surveys of magnetic fields in a sample of star-forming regions (Rao et al. 1998; Cortes et al. 2005; Zhang et al. 2014b; Hull et al. 2014). The arrival of the Atacama Large Millimeter/

submillimeter Array (ALMA) and the James Clerk Maxwell Telescope (JCMT) JMCT-Pol2, further improve the understanding of the effects of magnetic fields in star-forming regions (Pattle et al. 2023). However, a complete understanding of their effects is still elusive. This is particularly evident when studying the formation of high-mass stars (over $8 M_{\odot}$) because of their relative faraway distances and the complexity inherent to the high-mass star formation process. Through the detection of polarized emission from dust, where the main assumption is that dust grains are aligned by magnetic fields, detailed projected magnetic field morphology maps have been uncovered by ALMA from a number of high-mass star-forming regions (e.g., Cortes et al. 2016; Beltrán et al. 2019; Liu et al. 2020; Cortes et al. 2021a; Cortés et al. 2021b; Fernández-López et al. 2021; Sanhueza et al. 2021; Liu et al. 2023a, 2023b; Beuther et al. 2024). Here, we delve into the magnetic environment surrounding one of these high-mass star-forming clumps, NGC6334I, as part of the Magnetic fields in Massive star-forming Regions (MagMar) collaboration (P. Sanhueza 2024, in preparation). NGC6334I is a part of the vast giant molecular cloud (GMC) NGC6334, situated within the Sagittarius–Carina spiral arm, approximately 1.3 ± 0.3 kpc away from the Sun (Chibueze et al. 2014). Despite NGC6334's vastness (~ 100 pc), the regions of NGC6334I and NGC6334I(N) concentrate most of the studies in the millimeter and submillimeter range of the spectrum (McCutcheon et al. 2000; Hunter et al. 2014, 2017; Sadaghiani et al. 2020). A notable characteristic of NGC6334I is a significant millimeter flux outburst, predominantly centered on the MM1B protostellar core (Brogan et al. 2016; Hunter et al. 2017; Brogan et al. 2018; Hunter et al. 2018). This flux surge was accompanied by a flare in multiple maser species, particularly the OH maser transition which offered insights into line-of-sight magnetic field strengths (MacLeod et al. 2018). Moreover, several methanol maser lines, some previously unobserved, flared around the MM1 protocluster, hinting at a possible accretion event. Furthermore, outflow emission is also observed throughout NGC6334I. Initially detected in CO by Bachiller & Cernicharo (1990) using the IRAM 30 meter telescope, outflow emission was later observed in CS by McCutcheon et al. (2000) using the JCMT, and by Beuther et al. (2008) in HCN using the Australian Compact Array. Later, ALMA observations of CS ($J = 6 \rightarrow 5$) spatially resolved the emission finding four bipolar outflows where the most prominent one appears to originate from the MM1 protocluster (Brogan et al. 2018). Finally, the magnetic field in NGC6334I has been mapped by the SMA (Zhang et al. 2014a, 2014c; Li et al. 2015), the JCMT-Pol2 instrument at $14''$ resolution (Arzoumanian et al. 2021) and by ALMA at ~ 1.4 mm (220 GHz) and $0''.6$ resolution (Liu et al. 2023b). Here, we present 1.2 mm (250 GHz) and $0''.4$ resolution mapping of the magnetic field in NGC6334I. The ensuing sections are structured as follows. Section 2 outlines the observation techniques, calibration, and data analysis methods. Section 3 unveils the results from the polarized dust emission. Section 4 presents the discussion. We encapsulate our findings and conclusions in Section 5.

2. Observations

NGC6334I was observed as part of project 2018.1.00105.S, which was executed twice in the session mode (see Chapter 8

in Cortes et al. 2023, for details about the session observing mode), on 2018 December 13 and on 2019 May 4 under configuration C43-4 (providing baseline lengths from 15 to 783 m). The correlator was configured to yield full polarization cross correlations (XX , XY , YX , and YY) using the frequency division mode, including spectral windows to map the dust continuum and windows centered on a number of molecular line rotational transitions relevant to the study of high-mass star formation (see Table 1), with an effective wavelength of 1.2 mm. The bandpass was calibrated using J1427-4206 for session 1 and J1924-2914 for session 2. The time-dependent gain and the instrumental polarization terms were calibrated using J1717-3342 and J1751 + 0939, respectively. For the calibration, we used CASA version 5.4 and version 5.6 for imaging (CASA Team et al. 2022). To image the continuum, we manually extracted the line-free channels from each spectral window, which we later phase-only self-calibrated using a final solution interval of 90 s. These solutions were then applied to all of the molecular line transitions presented here before imaging. The spectral cubes were produced by using a 2 km s^{-1} channel width. The statistics of the flat Stokes images, before debiasing, for both continuum and channel maps are shown in Table 2. All of the Stokes parameters were imaged independently using the CASA task *tclean*, which yielded an angular resolution of approximately $0''.5 \times 0''.3$, with a position angle of -78° . The data were primary beam corrected and debiased pixel-by-pixel following Wardle & Kronberg (1974) and Hull & Plambeck (2015). Finally, we also obtained archival data from project 2017.1.00793.S, which also observed NGC6334I, but using a lower frequency spectral setup with an effective wavelength of 1.3 mm (see Liu et al. 2023, and Table 1). These data were also obtained in two sessions on 2018 June 28 and 2018 September 2, roughly two months apart. We did not combine these data sets, but briefly compared the polarized dust emission (see Section 3 and Appendix A).

3. Results

3.1. The Dust Continuum Emission

Figure 1 shows the NGC6334I total intensity (Stokes I) map from the ALMA 1.2 mm continuum data. The most massive sources previously identified by Brogan et al. (2016) are detected and indicated by blue crosses in the map. The dust continuum map at 250 GHz is also consistent with the lower frequency data obtained by Liu et al. (2023b; see Appendix A). The massive protocluster MM1 is not resolved in our data; nonetheless, we have superposed the individual peaks identified by Brogan et al. (2016) following their nomenclature and position. The unusual source CM2, a strong water maser source with an ambiguous origin and also detected in the radio continuum, is also seen in our data at the 30σ level of dust emission, where $\sigma = 1.0 \text{ mJy beam}^{-1}$ (see Table 2 and Tables in Brogan et al. 2016). The UC H II region from the MM3 core is well constrained, which gives us confidence that most of the emission at 250 GHz is coming from dust grains.

Since our data were acquired by executing two sessions separated by roughly five months, we explored the flux variability reported by Hunter et al. (2021), and references therein. To this effect, we imaged each session independently in all Stokes. We found that the differences between the flux in the MM1 protocluster were below 1%, below the ALMA

Table 1
Spectral Setup

Band	Spw 1 (GHz)	$\Delta\nu_1$ (kHz)	Spw 2 (GHz)	$\Delta\nu_2$ (kHz)	Spw 3 (GHz)	$\Delta\nu_3$ (kHz)	Spw 4 (GHz)	$\Delta\nu_4$ (kHz)	Spw 5 (GHz)	$\Delta\nu_5$ (kHz)	Spw 6 (GHz)	$\Delta\nu_6$ (kHz)	Spw 7 (GHz)	$\Delta\nu_7$ (kHz)	B_{maj} (arcsec)	B_{min} (arcsec)	PA (deg)
6	261.245	244	260.277	244.141	257.523	976	245.520	976	243.520	976	0.45	0.4	-82.8
6	216.430	976	218.54	976	233.54	976	230.528	122	231.051	122	231.211	122	231.312	122	1.7	1.1	87
6	216.430	976	218.54	976	233.54	976	230.528	122	231.051	122	231.211	122	231.312	122	0.7	0.5	68

Note. The spectral configuration and beam sizes from the MagMaR project (row 1) are detailed here along with the configuration used by project 2017.1.00793.S (rows 2 and 3). For each spectral window (e.g., Spw 1), the center frequency is indicated in GHz, along with the channel width in kHz (e.g., $\Delta\nu_1$). The synthesized beam parameters (angular resolution) for both projects are the major axis B_{maj} , minor axis B_{min} , and position angle PA. Note that project 2017.1.00793.S was observed in two different configurations hence the two different beam sizes between rows 2 and 3.

Table 2
Continuum Images Statistics

Stokes	Max (mJy beam ⁻¹)	Mean (mJy beam ⁻¹)	σ (μ Jy beam ⁻¹)
I	1300	33.0	998
Q	4.1	-0.01	55
U	4.1	0.07	55
V	1.6	0.03	76

Note. The Stokes Images statistics, from the combined sessions, are listed here. Note that Stokes *I* is dynamic range limited; also, Stokes *Q*, *U*, and *V* can be negative, and thus, the maximum is not necessarily a positive value. Furthermore, note that the units of Stokes *Q*, *U*, and *V* are σ are μ Jy beam⁻¹. The Stokes *V* values from ALMA observations are subject to larger uncertainties than linear polarization (see Cortes et al. 2023).

accuracy of band 6 ($\sim 10\%$). Because the 2017.1.00793 data (220 GHz) were taken on different configurations and only ~ 2 months apart, comparing the two is difficult therefore we omit it from here on. We also explored variability in the polarized flux where we found variability in Stokes *Q* and *U* on the order of 8% (see Table 3). Note that the minimum amount of detectable linear polarization by ALMA is estimated to be 0.1%, as established from point source measurements (Cortés et al. 2023). Because the flux variability in Stokes *I* during this period was negligible, this suggests that the outburst might have already finished or the emission is below our sensitivity. Although a variability of 8% in *Q* and *U* within six months appears intriguing, its analysis is out of the scope of this work and we defer it to a future investigation.

3.2. Column Density and Mass

Calculating the column density from dust emission at millimeter wavelength is a well-established procedure. Here, we use the standard formulation developed by Hildebrand (1983) but we make use of the NGC6334I temperature model obtained by Liu et al. (2023b) from Methanol emission where we assume that the gas emission is optically thin and that the gas and dust are in thermal equilibrium (see Figure 2). The temperature model map was extended to match the dust emission spatial distribution detected by ALMA to the 3σ level. To extend the model temperature map, we assumed that the dust temperature converged to 30 K outside the original model map. This is justified given the results from McCutcheon et al. (2000) and Sandell (2000) who derived a dust temperature value of 30 K for NGC6334I using all available millimeter and millimeter data at the time. The map was later smoothed using a Savitzky–Golay smoothing filter (Savitzky & Golay 1964) with a window of one beam to ensure continuity.²³ Besides the temperature model, we used a dust emissivity $\kappa_{\nu} = 1 \text{ cm}^2 \text{ gr}^{-1}$ for the dust grains at 230 GHz (Ossenkopf & Henning 1994), and a gas-to-dust ratio of 100 and the assumption that the dust emission is optically thin. The column density map in log scale is shown in Figure 2. Note, because the temperature model derived by Liu et al. (2023b) may have used optically thick

²³ The Savitzky–Golay filter is a digital filter that can be applied to a set of digital data points for the purpose of smoothing the data. This is achieved by fitting successive subsets of adjacent data points with a low-degree polynomial by the method of linear least squares. We use this filter to smooth the temperature map because the filter is particularly useful to preserve important features of the data, such as relative maxima, minima, and width, which are often “washed out” by other types of smoothing filters.

CH₃OH emission, we may be overestimating the temperature in the most dense regions of the clump, which would lead to underestimations of the column density. Nonetheless, the column density values at the core positions in our map appear to be in agreement with Brogan et al. (2016) who observed NGC6334I with ALMA and the Very Large Array computing the spectral energy distributions (SEDs) for the major sources in the region deriving temperatures and densities. By having a column density map,²⁴ we can estimate a map of the mass. We do this by computing $m_{i,j} = \mu m_{\text{H}} N_{i,j} A$, where i, j are map pixel indexes along R.A. and decl., respectively, A is the area of each pixel, m_{H} is the mass of Hydrogen, $\mu = 2.8$ is the mean molecular weight, and $N_{i,j}$ is the column density per pixel.

3.2.1. The Number Density Map

Because of the complicated morphological features seen in the dust emission, it is difficult to model the spatial distribution of the dust and determine its volume density. A simple approach is to assume that the whole region is a cylinder of a certain thickness, which can be estimated from the dust emission intensity profile. Opting for a cylindrical rather than spherical geometry could be more appropriate for several reasons. While a spherical model encompassing all dust emission at the 3σ level indicates a mean radius of approximately 0.02 pc, leading to average and peak number densities significantly lower than those observed in ALMA studies of the region, a cylindrical model offers more flexibility. By adjusting the cylinder’s height, it becomes possible to align the modeled core densities more closely with the observed densities ranging between 10^7 and 10^{10} cm^{-3} , as reported by Brogan et al. (2016) and Sadaghiani et al. (2020). This approach allows for a more accurate representation of the physical conditions within these dense cores. Note that this simple geometrical assumption assumes the same height throughout NGC6334I, which is not accurate. It is more likely that the cores in this region will follow a power-law density profile different from the rest of the surrounding gas. Thus, we choose the height of the cylinder looking for a drop in the intensity as a function of the distance from the peak emission and assume that this length corresponds to the height. The number density per pixel is determined then by computing $n_{i,j} = N_{i,j}/Z$, where Z is the thickness of the cylinder. By doing this, we find a drop in the intensity at the 5σ level in the dust emission which corresponds to $\sim 5''$ or 0.03 pc at a distance of 1300 pc. The values presented in our number density map align with those established by Brogan et al. (2016), which were derived from SED fitting to ascertain dust temperatures and under the assumption of spherical geometry.

3.3. The Magnetic Field Morphology from Polarized Dust Emission

Figure 3 displays the magnetic field morphology on the plane of the sky, derived from polarized dust emission under the assumption of grain alignment by magnetic fields (Lazarian & Hoang 2007), which assumes a 90° rotation in the linear polarization position angle. While alternative alignment mechanisms such as radiative alignment (Tazaki et al. 2017)

²⁴ Note that we are deriving here a magnetic field map that has values per pixel. However, the limiting resolution factor is given by the synthesized beam of the telescope which should be taken into account when deriving conclusions from these maps.

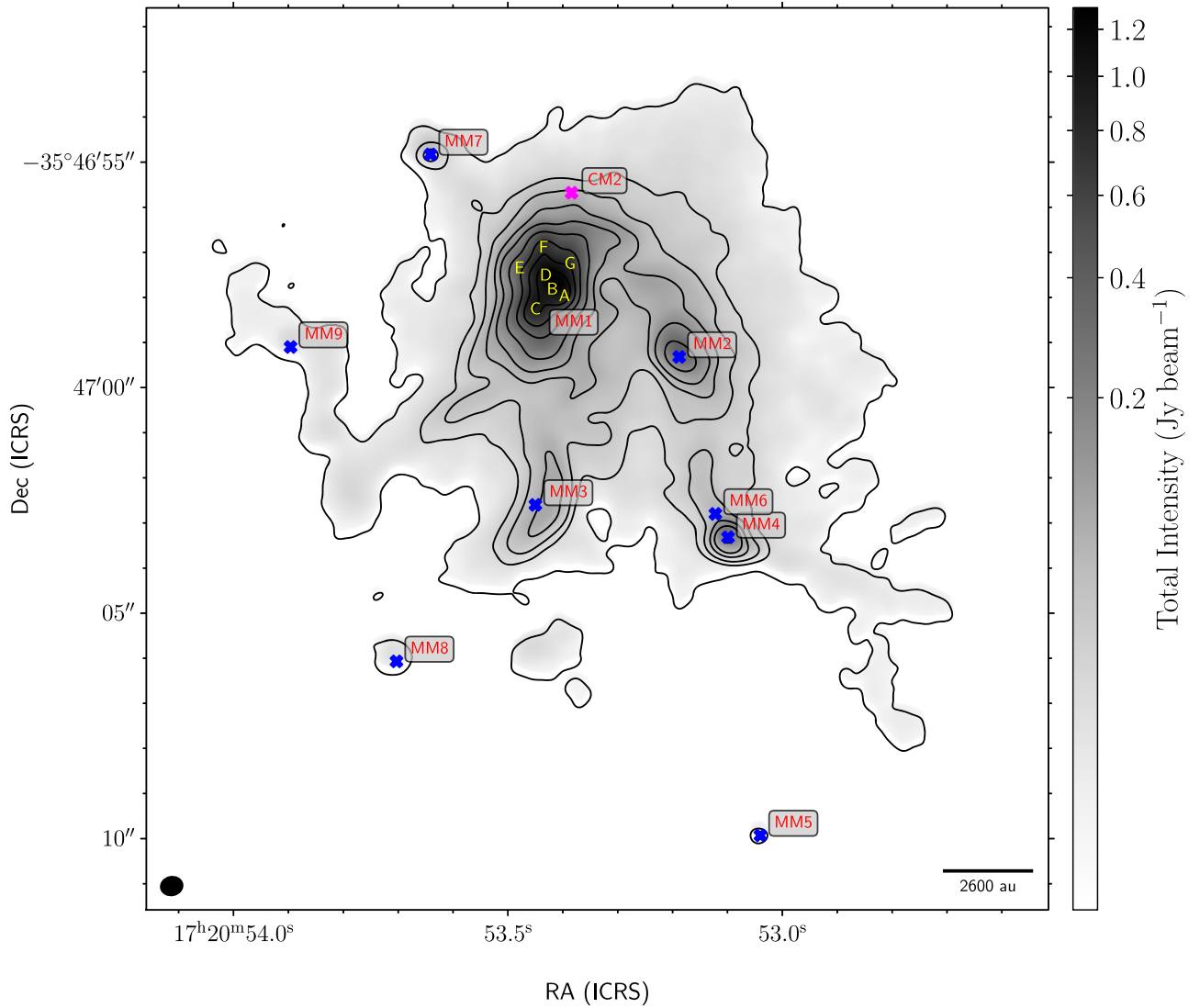


Figure 1. This figure displays the 1.2 mm total intensity dust emission from NGC6334I. The gray scale indicates the intensity in Jy beam^{-1} , corresponding to the scale bar on the right. Contours represent intensity levels at 3.6, 18, 36, 72, 120, 240, 480, 720, and 960 mJy beam^{-1} . Sources within our field of view, previously detected by Brogan et al. (2016), are marked with blue crosses and labeled in red. Notably, the MM1 source has shown signs of fragmentation, potentially forming a protocluster. The letters A through G denote the MM1 peak regions as identified by high-resolution ALMA observations. The magenta cross shows the position of the CM2 synchrotron/maser source, the bar at the bottom right corresponds to a length scale of 2600au, and the beam size of our ALMA image using $\text{robust} = 0.5$ is shown by the black ellipse to the bottom left.

Table 3
Flux Variability

Stokes	Max_{s1} (mJy beam^{-1})	Mean_{s1} (mJy beam^{-1})	σ_{s1} (mJy beam^{-1})	Max_{s2} (mJy beam^{-1})	Mean_{s2} (mJy beam^{-1})	σ_{s2} (mJy beam^{-1})	variability (%)
I	1330	45	0.988	1331	42	1.0	0.1
Q	3.91	0.028	0.067	4.3	-0.007	0.073	8
U	3.97	0.075	0.083	4.3	0.088	0.068	8
V	-1.06	-0.003	0.083	2.8	0.06	0.100	...

Note. The flux density variability for all Stokes continuum images is listed here. The values were extracted from the images considering the 1/3 FWHM for the maximum and the mean while we used a region devoid of emission for σ . The subscripts s1 and s2 indicate session 1 and session 2. Note that Stokes Q , U , and V can be negative, and thus, the maximum is not necessarily a positive value. We do not list the variability in Stokes V due to the large ALMA uncertainties with circular polarization.

and self-scattering (Kataoka et al. 2016) have been proposed, the scales and physical conditions in massive star-forming regions (like the radiation anisotropy and large grain sizes), make them less favored. Consequently, magnetic alignment

emerges as the most probable process driving the polarized emission detected toward NGC6334I. The polarized emission encompasses most of the primary sources in NGC6334I, including MM1, MM2, MM4, MM6, MM7, MM9, and CM2

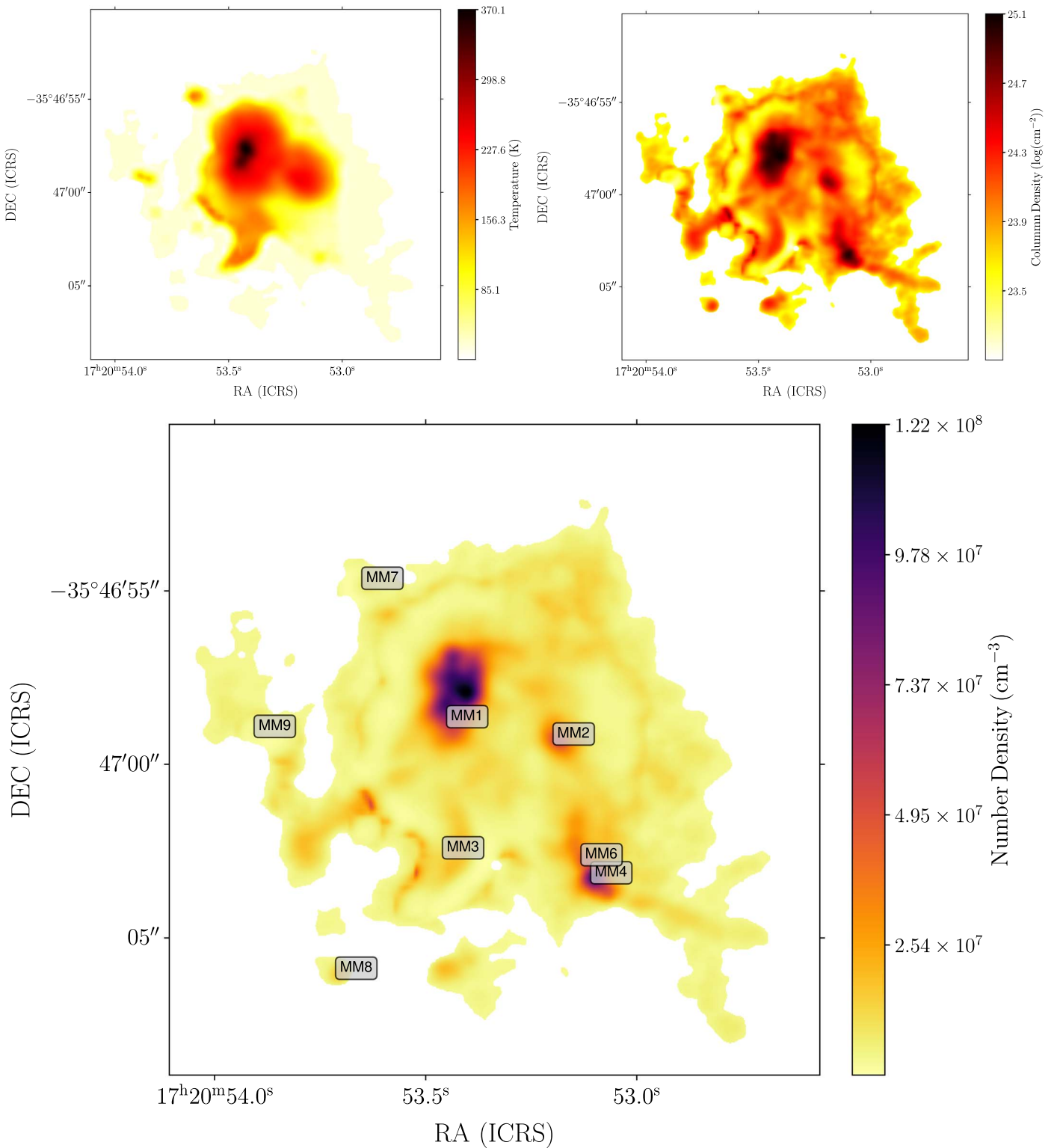


Figure 2. (Top) The extended temperature model map from (Liu et al. 2023) is shown here in color scale indicating dust the temperature throughout NGC6334I along with column density map in logarithmic scale derived by using the temperature model map. (Bottom) The number density map is derived by assuming cylindrical geometry and a thickness of 0.03 pc. The main sources identified by Brogan et al. (2016) are indicated in the map with their respective labels.

(a strong water maser source with an ambiguous origin). Notably, the cometary UC H II region MM3 lacks significant polarized dust emission, thus leaving its magnetic field untraced (refer to Figure 1 in Sadaghiani et al. 2020, for the extent of the MM3 UC H II). The field morphology, albeit intricate, reveals consistent patterns across certain directions.

For instance, the field demonstrates an evolution from north-west (NW) to southeast (SE), showing discernible changes over the fragmented MM1 core, possibly a radial morphology toward the MM1 center of mass (see Figure 4). Similarly, indications of radial configurations in the field lines can also be seen around the MM2 and MM4/MM6 cores. Radial

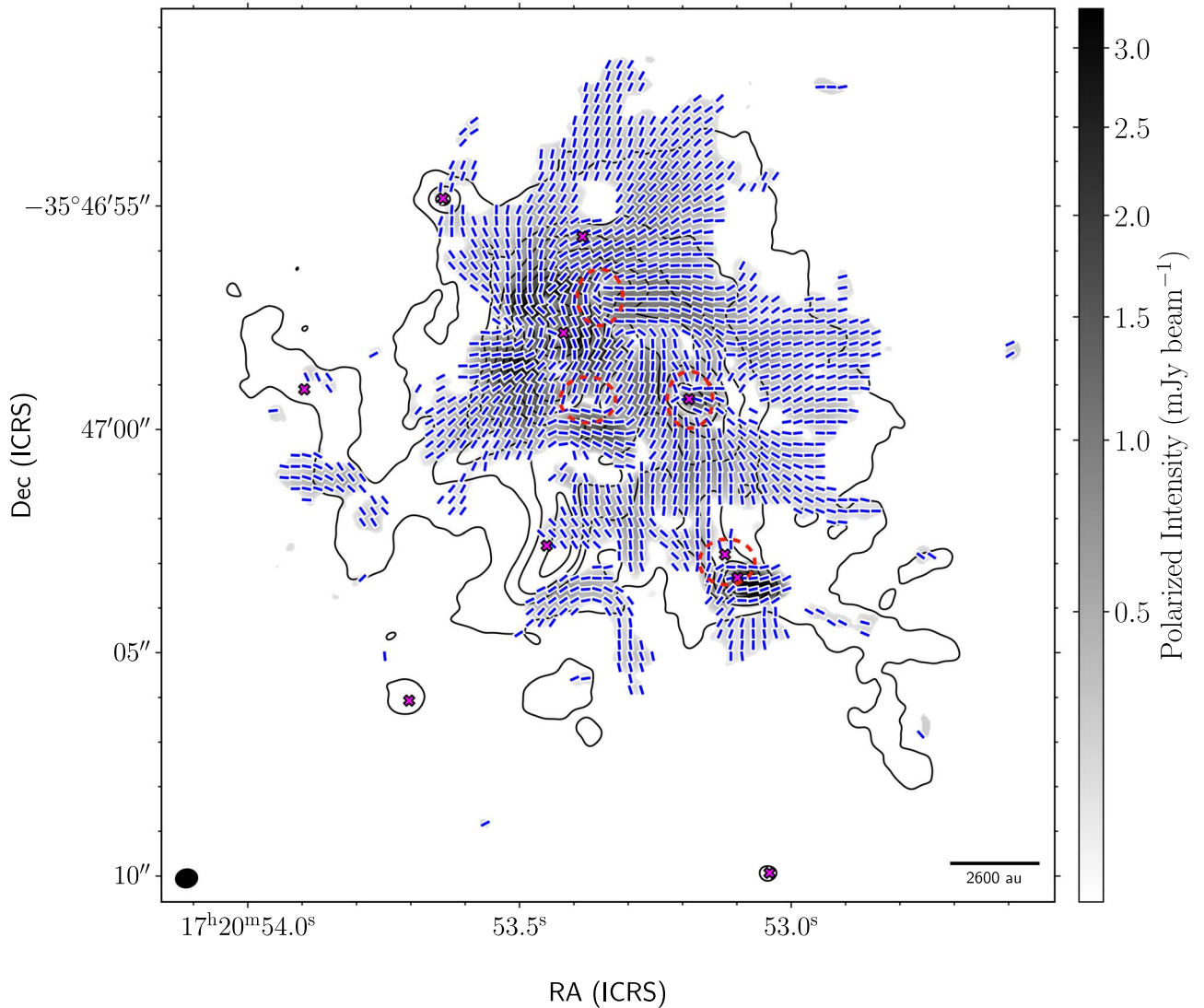


Figure 3. The figure illustrates the magnetic field morphology in NGC6334I, represented by blue pseudovectors. These are derived from a 90° rotation of the linearly polarized dust emission at 250 GHz, assuming the grains are aligned with the magnetic field. Pixel-level debiasing has been applied to the polarized emission at the 3σ level. The resolution of the observation is indicated by the black ellipse in the lower left corner, representing the synthesized beam, while the scale bar in the lower right corner corresponds to an angular scale of $2''$, or 2600 au. Positions of key sources are marked with magenta crosses and regions where the field appears to turn by 90° are indicated by red segmented ellipses.

morphologies suggest that gravity dominates and drags the field toward the center of mass (Tang et al. 2009; Girart et al. 2013; Cortes et al. 2016; Koch et al. 2018; Cortes et al. 2019; Koch et al. 2022). Noteworthy discontinuities, such as roughly 90° shifts in field direction between adjacent pseudovectors, appear at the fringes of MM1 over the MM2 core and between MM6 and MM1. Despite these discrepancies, the field predominantly appears coherent on scales of $5''$ – $10''$ (equivalent to 6500–13,000 au, as visualized in Figures 1 and 3). Spiral field patterns, like those observed in G327 and IRAS 18089 (Beuther et al. 2020; Sanhueza et al. 2021), where spiral attributes are conspicuous and where rotation and infall have been deemed dynamically significant, may be present in the inner regions of the MM1 protocluster (see Figure 4). However, clear rotation signatures are not conclusive from our data. Nonetheless, small-scale spiral patterns have been observed in other high-mass sources. Burns et al. (2023) observed spiral signatures on the also outbursting source G358.93-0.03-MM1 from high-spatial-resolution (50 – 900 au), 6.7 GHz methanol

maser emission. Based on these results, it is plausible that, in NGC6334I, the indications of spiral morphologies seen in the field are retained in the gas but not resolved due to the limitations of the ALMA configuration used here.

3.4. Molecular Line Emission

The spectral setup used by the MagMaR project allows for the detection of molecular line emission from a number of tracers usually abundant in high-mass star-forming regions. From our data, we used $\text{CS}(J=5 \rightarrow 4)$ and $\text{C}^{33}\text{S}(J=5 \rightarrow 4)$ to study outflow and nonthermal motions. From the data obtained by Liu et al. (2023b), we extracted the $^{12}\text{CO}(J=2 \rightarrow 1)$ emission, which we used to study the outflows present in NGC6334I.

3.4.1. The $\text{CS}(J=5 \rightarrow 4)$ Emission

Figure 5 displays a moment-zero map of the $\text{CS}(J=5 \rightarrow 4)$ emission toward NGC6334I, where the data have been

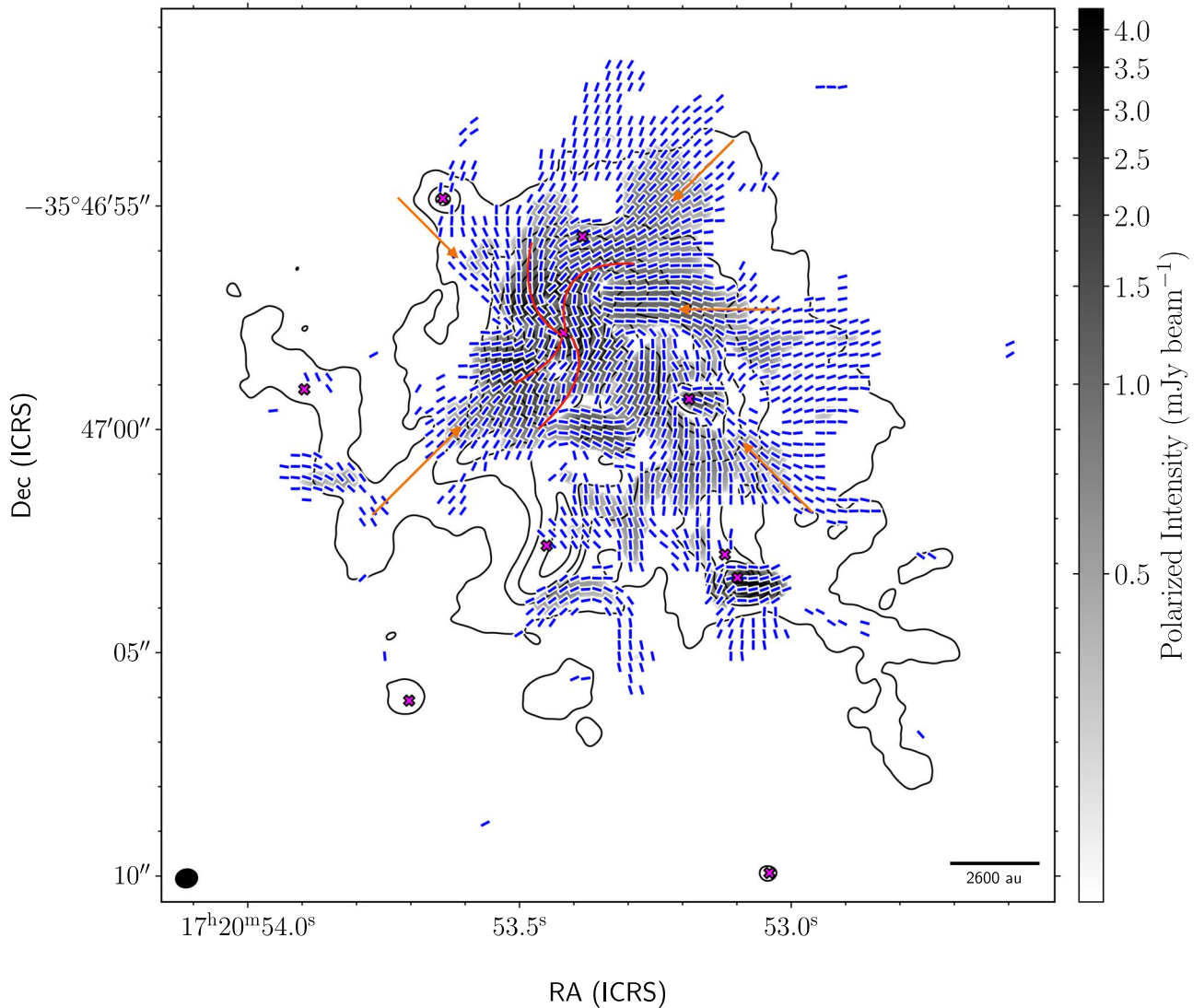


Figure 4. Same as Figure 3, but here we indicate possible preferred directions of the field projected onto the plane of the sky. The orange arrow indicates the radial direction toward the center of mass, the MM1 protocluster. The red lines indicate possible spiral arms at the center of the MM1 protocluster in NGC6334I.

categorized into redshifted and blueshifted velocity components to show outflow emission. This categorization was done by considering a systemic velocity of -7.56 km s^{-1} , as determined by a Gaussian fit to the C^{33}S line (refer to Section 3.4.2), with velocity intervals of -40 to -12 km s^{-1} for the blueshifted and -4 to -12 km s^{-1} for the redshifted components. Outflow emission is clearly seen in the CS moment-zero map, where our data align with the morphological findings of Brogan et al. (2018). Following their nomenclature, our map reproduces the prominent northeast (NE)–southwest (SW), the MM1B north–south (N–S), the MM1B NW, and the MM4 SE–NW outflow emissions as indicated in Figure 5. From the four outflows detected toward NGC6334I, the NE–SW outflow appears to be dominant. Although its exact origin has not been conclusively determined, it appears to emerge from the MM1 protocluster, which is also the likely origin of the smaller MM1B N–S and MM1B NW outflows. From the map, the NE–SW outflow red lobe appears to be carving a cavity in the dust as shown in Figure 5. The edges of this cavity seem to be traced by magnetic fields as we will show later (see Section 4). To study the CS emission in

more detail, we modeled the data using the MADCUBA package which fits spectroscopy models to the data using a complete radiative transfer formalism under local thermodynamic equilibrium assumptions (Martín et al. 2019). To this effect, we extracted a spectrum from the central region of NGC6334I containing the CS line and a number of other molecular transitions (see Table 1 for a description of the spectral windows containing the CS line). This spectrum was modeled with the MADCUBA package where we found that the CS line would be optically thick ($\tau=6$) assuming an excitation temperature $T_{\text{ex}} = 260 \pm 20 \text{ K}$ derived with available transitions of CH_3OH , $^{13}\text{CH}_3\text{OH}$, and $\text{C}_2\text{H}_5\text{OH}$ in the observed spectral windows, and based on the C^{33}S fit and assuming a $^{32}\text{S}/^{33}\text{S} = 102$ taken from (Yu et al. 2020) since the CS profile is heavily affected by self-absorption.

3.4.2. The $\text{C}^{33}\text{S}(J=5 \rightarrow 4)$ Emission

The $\text{C}^{33}\text{S}(J=5 \rightarrow 4)$ emission appears to be compact and confined to the brightest dust emission contours, as shown in Figure 6. The peaks in the integrated intensity map coincide with the dust emission peaks while most of the C^{33}S is confined

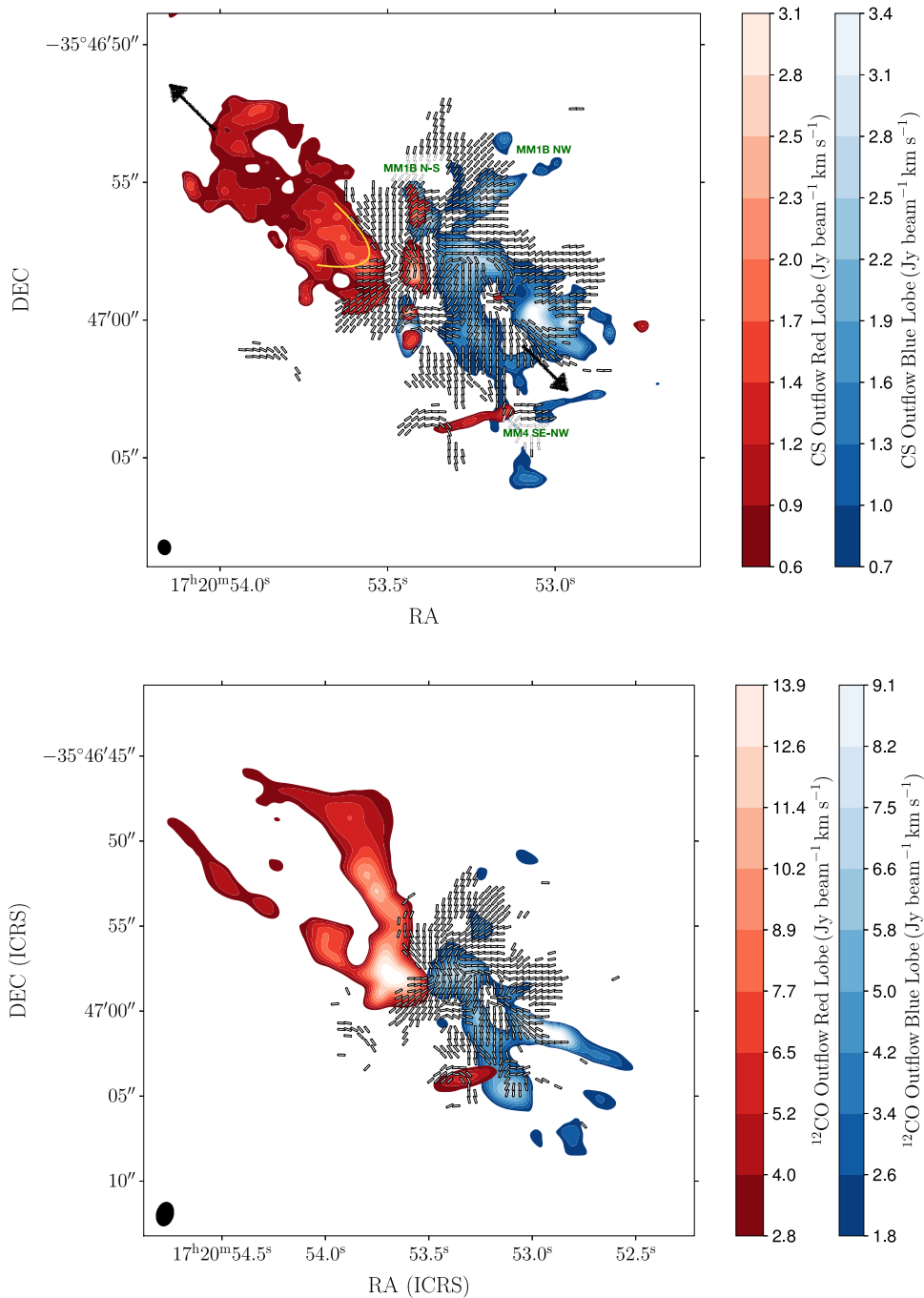


Figure 5. Top: CS($J = 5 \rightarrow 4$) emission from NGC6334I’s outflows with the magnetic field overlaid. Blue and red lobes are derived from velocities -40 to -12 km s^{-1} and -4 to 12 km s^{-1} , respectively. The outflow cavity is outlined in yellow, with individual flows labeled per Brogan et al. (2018) and the primary NE–SW flow indicated by arrows. Bottom: CO($J = 2 \rightarrow 1$) emission tracing NGC6334I’s outflows with the magnetic field overlaid. Blue and red lobes span from -45 to -25 km s^{-1} and -4 to 11 km s^{-1} , respectively. The CO emission also reveals the cavity, with the magnetic field contouring the outflow’s edges.

within the 15σ contour from the dust emission. While the MM1 protocluster is not resolved in the dust emission, three distinct condensations are observable in C^{33}S from north to south and around the dust peak, which are loosely associated with the condensations resolved by the higher resolution ALMA data (Brogan et al. 2016) as indicated by the white crosses in Figure 6. Toward MM2, the C^{33}S peak emission aligns well with the dust maxima, whereas the emission levels appear marginal toward MM4 and MM7, and remain undetected toward MM9. In Figure 6, the moment-one map is also presented, relative to $V_{\text{lsr}} = -7.56$, km s^{-1} , obtained through

Gaussian fitting of the C^{33}S spectrum from the $1/3$ FWHM of the primary beam. From this map, a velocity gradient is seen from NE to SW, which is consistent with that obtained by Liu et al. (2023b) using the OCS molecular emission, though our coverage does not match the extent of the ALMA mosaic in Liu et al. (2023b). Although the velocity gradient might have some outflow contamination, the spectra shown in Figure 6 suggest it should be minimal. This is because the C^{33}S line profile is almost completely Gaussian with very small deviations around the -20 km s^{-1} velocity channel. Thanks to the lack of absorption features, we could fit the C^{33}S spectrum with the

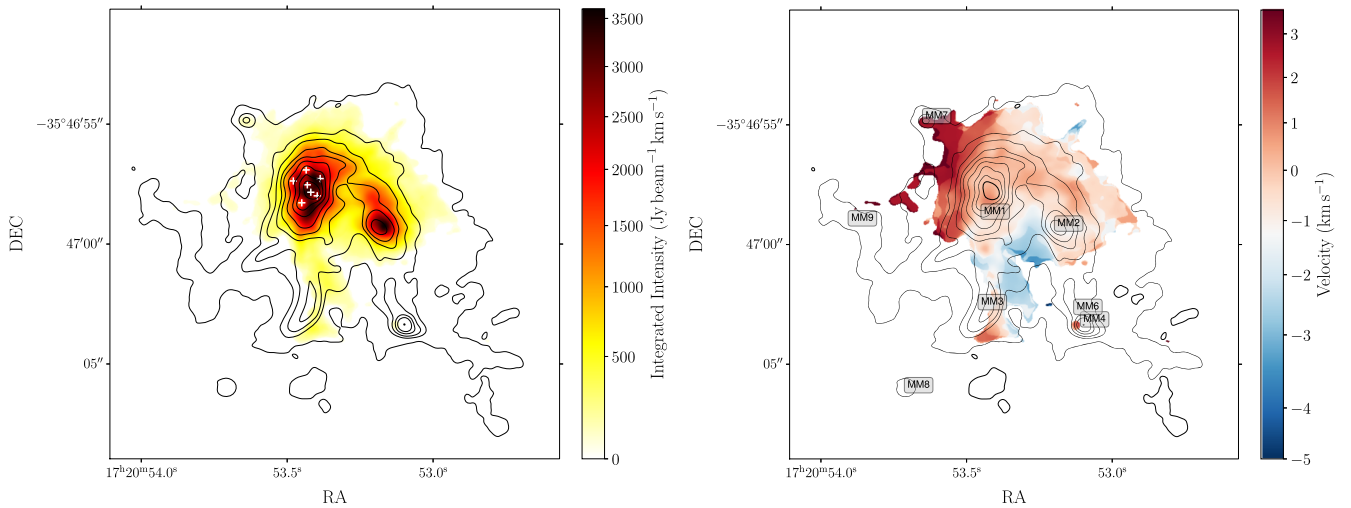


Figure 6. The figure shows to the left the $C^{33}S$ moment-zero map in color scale with superposed contours from dust emission starting at the 3σ level (see Figure 1). The white crosses correspond to the MM1 protocluster condensations resolved by Brogan et al. (2016). To the right, we show the moment-one map in color scale, also with dust continuum contours superposed, as $\Delta V_{ij} = V_{ij} - V_{lsr}$, where $V_{lsr} = -7.56$ is the velocity center of the $C^{33}S$ line as determined by a Gaussian fit.

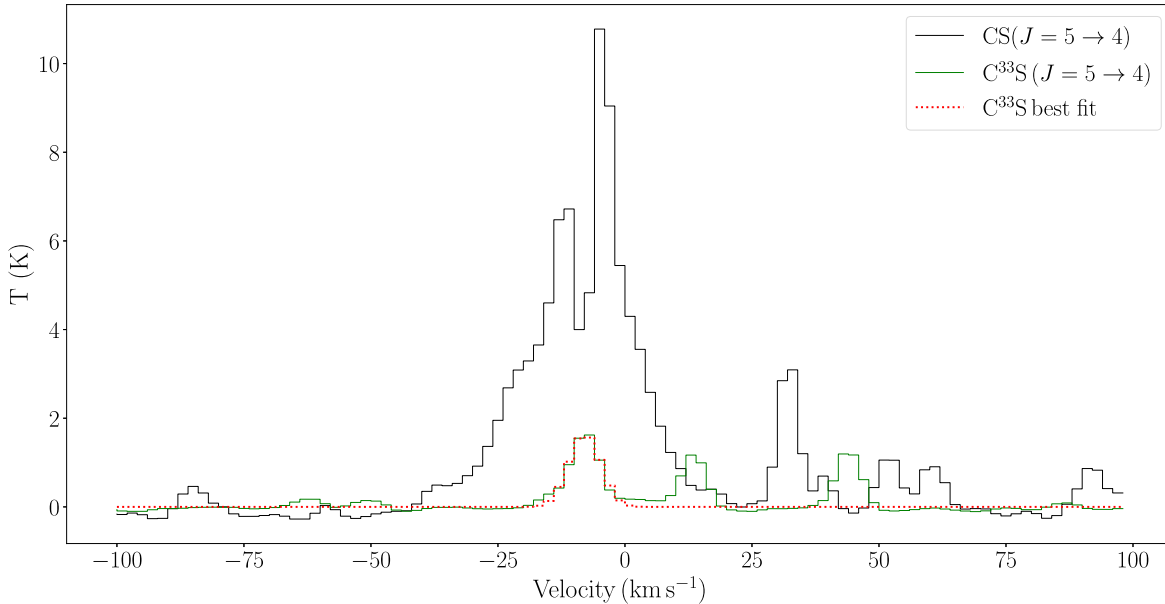


Figure 7. The figure shows spectra from CS ($J = 5 \rightarrow 4$) (black), $C^{33}S$ ($J = 5 \rightarrow 4$) emission (green), and its best Gaussian fit (red dotted line) extracted from an area covering the outflow emission seen from CS moment-zero map. The other two spectral features seen in the $C^{33}S$ spectrum correspond to methyl formate emission (similar to what was seen in NGC6634I(N), see Cortés et al. 2021b).

same temperature assumption done for CS above, which suggests that the emission is optically thin ($\tau = 0.3$) which allows us to use the moment-two map as the velocity dispersion along the line of sight (see Figure 7).

3.4.3. The $^{12}CO(J = 2 \rightarrow 1)$ Emission

We used the ALMA data obtained by Liu et al. (2023b) to image the outflow emission from NGC6334I (see Table 1 for a description of their data). To image the outflow emission we used a velocity interval from -45 to -25 km s^{-1} for the blue lobe and -4 to 11 km s^{-1} for the red lobe (refer to Figure 5, which displays the combined data from both ALMA configurations). From these data, only the NE to SW outflow is clearly discernible, whereas the N–S outflow in the line of sight remains undetected in ^{12}CO and some traces of the MM1B NW outflows are seen in the blue

lobe. Additionally, only the red lobe of the MM4 outflow is observable in ^{12}CO . As with the CS emission, the red lobe of the CO outflow appears to be carving a cavity in the dust where the magnetic field traces the edges of the cavity (see Section 4). Although this data set includes configuration C41, the most compact ALMA configuration with a maximum recoverable scale of $\sim 9''$ (0.06 pc at 1300 pc, the distance to NGC6334I), there appears to be significant extended emission from ^{12}CO that the interferometer is resolving out. Figure 8 shows CO and CS spectra superposed to each other. Although the outflow emission is seen in both molecular profile line wings, the comparison suggests, as previously mentioned, that significant emission from CO is missing. This is likely either due to filtering effects or self-absorption (see Section 3.4.3). Therefore, we omit using CO emission for the outflow analysis here.

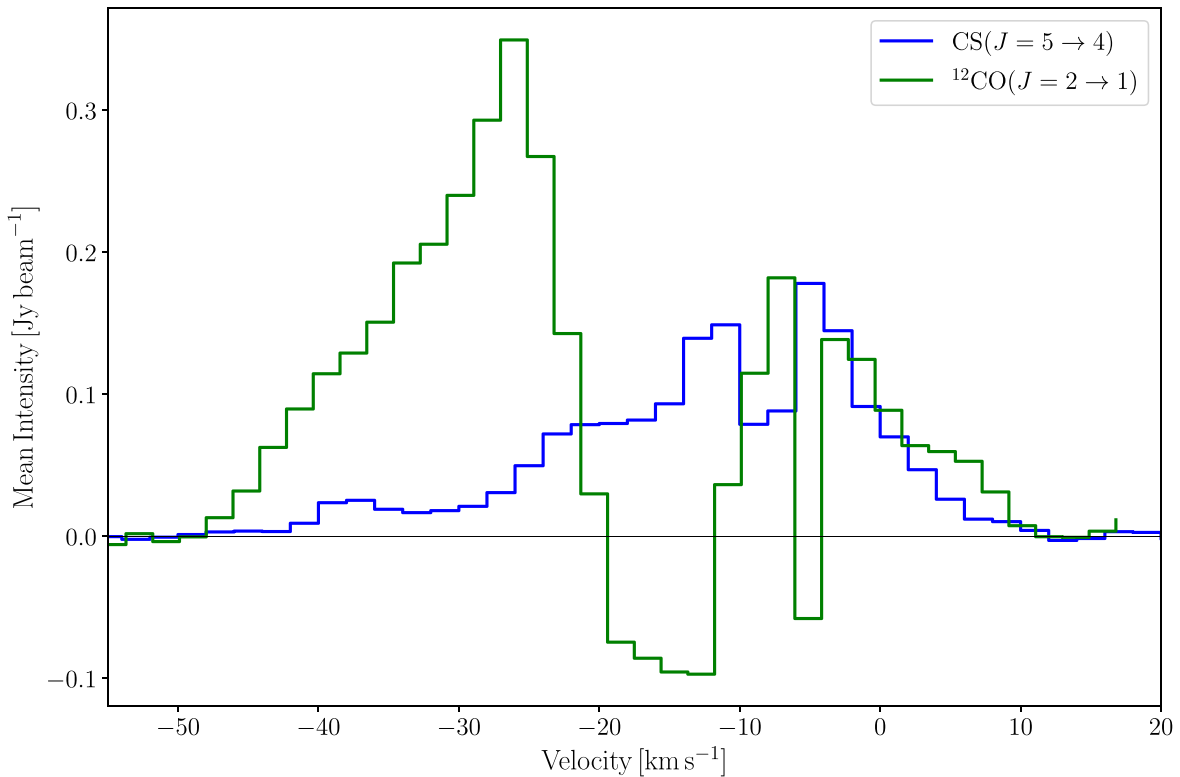


Figure 8. The figure shows spectra from the ^{12}CO ($J = 2 \rightarrow 1$) and CS ($J = 5 \rightarrow 4$) emission extracted as the mean within the $1/3$ FWHM of our maps, corresponding to 0.05 pc. The ^{12}CO spectrum was binned to match the velocity resolution of the CS spectrum at 2 km s^{-1} .

4. Discussion

At first glance, the magnetic field in NGC6334I displays a complex morphology that is difficult to associate with a projection from a simple shape, such as the “hourglass” proposed by models (Ciolek & Mouschovias 1994) and observed in numerous star-forming regions (Girart et al. 2006; Hull et al. 2014; Li et al. 2015; Beltrán et al. 2019; Cortés et al. 2021b). Although there are indications of a radial pattern at the outskirts of the clump and in the direction of the MM1 protocluster, there are also hints of some sort of spiral arms in the field close to the central region of the MM1 protocluster (see Figure 4). The radial pattern can be explained by a dominant gravitational pull, but for the spirals, we do not find conclusive evidence of rotation or velocity gradients that can explain these features in the field morphology at these scales (see Figure 6). Nonetheless, small-scale spiral patterns cannot be ruled out given previous findings in other similar high-mass outbursting sources (see Burns et al. 2023). Additional complexity in the field morphology arises from sudden 90° shifts in the field lines. These turns in the field morphology can be seen around the MM2 and MM6 cores, and also at the interface of the MM1 protocluster as indicated by the red ellipses in Figure 3. These sharp shifts in the field morphology are challenging to elucidate; they could result from projection effects or perturbations in the field by the gas due to turbulence or gravity. One possibility is that the four outflows detected in this region might be perturbing the magnetic field structure. For instance, the most prominent bipolar outflow, seen in both CO and CS emission red lobe, appears to carve a cavity in the dust where the magnetic field seems to follow the edges of the cavity as indicated in Figure 5. Similar situations have been seen in low-mass star-forming regions such as

Serpens SMM1-b where the outflow emission was also found to trace the edges at the base of the outflow cavity (Hull et al. 2017). We also note that the field shows some degree of alignment with the MM1B NW and the MM4 SE–NW outflows. However, whether this is a projection effect or real alignment cannot be concluded from these data. As understanding projection effects demands extensive numerical modeling, we instead examine whether the energy balance in NGC6334I could explain the perturbations seen in the field.

4.1. The Energy in the Outflows

To explore the quantitative effect of the outflow in the magnetic field, we attempt here to compute the outflow parameters in order to estimate their total energy. To derive the energy in the outflows, we used the CS emission rather than the CO emission. This is because the CO emission shows, what appears to be, significant filtering by the interferometer and possibly extensive self-absorption which will introduce larger errors in the estimations. Also, the CS line appears to better trace the outflows at the core scales mostly resolving all four outflows while the CO does not clearly show all of the outflow emission detected in NGC6334I (see Figure 5). However, it should be noted that because the interferometer does not recover all of the CS emission and because of the uncertainties in the abundance ratio between CS and H_2 , the outflow parameters derived here may have a large uncertainty. To estimate the outflow parameters, we extracted spectra from the CS velocity cube covering the extent of the CS moment-zero map (see Figure 7). Determining the outflow parameters requires separating the emission coming from the gas at the source systemic velocity and the actual emission from the outflow. It also requires estimating the optical depth in the line

wings, which is usually done by computing the line ratio with an isotopologue that has sufficient overlap in the line wings covering the outflow emission. Unfortunately, the $C^{33}S$ emission detected toward NGC6334I is compact enough that the overlap with the CS at velocities associated with the outflow is minimal (see Figure 7). Thus, to estimate the CS column density corresponding to the outflow emission, we assume that this emission is optically thin in the channels covering the CS line wings. The line wings of the CS line cover the interval from -40 to -12 km s^{-1} for the blue lobe and -2 to 20 km s^{-1} for the red lobe where the systemic velocity of the source is determined to be -7.6 km s^{-1} as obtained from the Gaussian fit to the $C^{33}S$ line (see Figure 7). This interval covers all of the emission in the line wings over 3σ , with $\sigma = 0.2$ K estimated from 25 line-free channels. Note, we are not aiming to characterize independently the four outflows in this region, but rather estimate their bulk energy and its effect on the magnetic field.

By assuming that the emission is optically thin, we estimate the CS column density per velocity channel as (see Equation (16), Zhang et al. 2016),

$$N = \left(\frac{8\pi k \nu_{ul}^2}{hc^3 A_{ul} g_u} \right) \frac{T_R(\nu)}{f} Q_{\text{rot}}(T_{\text{ex}}) \delta v e^{\frac{E_u}{kT_{\text{ex}}}}, \quad (1)$$

where k is the Boltzmann constant, h is the Planck constant, c is the speed of light in the vacuum, $\nu_{ul} = 244.9355565$ GHz is the rest frequency of the $J=5 \rightarrow 4$ CS rotational transition, $A_{ul} = 2.981 \times 10^{-4} \text{ s}^{-1}$ is the Einstein spontaneous emission coefficient, $g_u = 11$ is the statistical weight, $E_u = 35.3$ K is the energy level for the upper state, Q_{rot} is the partition function, which for linear molecules is well approximated by $Q_{\text{rot}} = \frac{kT_{\text{ex}}}{hB_0}$, where $B_0 = 24.5$ GHz is the rotational constant for the CS molecule (Bustreel et al. 1979), $\delta v = 2$ km s^{-1} is the channel width, and f is the beam filling factor assumed to be 1. As indicated in Section 3.4.1, the excitation temperature, $T_{\text{ex}} = 260$ K, is estimated from the modeling done with MADCUBA on symmetric rotor molecules. The mass of the outflow is calculated for every velocity channel as:

$$M = \mu_{\text{H}_2} m_{\text{H}} AN_{\text{H}_2}, \quad (2)$$

where $\mu_{\text{H}_2} = 2.8$ corresponds to the mean molecular weight (Feddersen et al. 2020), m_{H} is the Hydrogen mass, A is the area subtended by the region identified with the outflows (same used to extract the spectra from Figure 7), and $N_{\text{H}_2} = N/X_{\text{H}_2}^{\text{CS}}$ is the total column density of the molecular hydrogen, where $X_{\text{H}_2}^{\text{CS}} = 1.2 \times 10^{-7}$ is the relative abundance of CS respect to the H_2 in NGC6334I as determined from Herschel mapping (Zernickel et al. 2012). The momentum and kinetic energy per velocity channel are estimated as $P_i = M_i v_i$ and $E_i = M_i v_i^2/2$, where i indicates the velocity channel used for each quantity (in this case M_i is the mass spectrum, see Feddersen et al. 2020). The total mass, momentum, and energy are obtained by adding all velocity channels per lobe. The values for the mass energy and momentum are listed in Table 4. The assumption is that the CS emission is optically thin and the line wings appear to be good enough to produce underestimates of the total energy in the outflow when compared to single-dish results. McCutcheon et al. (2000) estimated the kinetic energy on each outflow lobe to be $\sim 1.4 \times 10^{47}$ erg from their CO and CS millimeter single-dish mapping while our estimates are an order of magnitude

Table 4
Outflow Parameters

Source	Lobe	M (M_{\odot})	P ($M_{\odot} \text{ km s}^{-1}$)	E (10^{46} erg)
NGC6334I	Blue	0.3	6.4	0.24
NGC6334I	Red	0.6	4.9	0.11

Note. The outflow parameters determined from the CS emission are presented here. The red lobe was obtained by considering a velocity range between -4 and 12 km s^{-1} while the blue lobe was obtained from a range between -40 and -12 km s^{-1} .

lower (see Table 4). Although the mass, momentum, and energy are consistent with outflow properties from surveys of high-mass protostellar outflows (Zhang et al. 2001, 2005), it should be noted that we are missing emission that might be present at the systemic velocity as well as the emission filtered out by the interferometer. Thus, the values derived here appear to be a lower bound for the outflow mass, momentum, and energy at these scales in NGC6334I.

4.2. The Magnetic Field Strength Map

To estimate the magnetic field strength on the plane of the sky, B_{pos} , we employed the Davis–Chandrasekhar–Fermi technique (DCF; Davis 1951; Chandrasekhar & Fermi 1953) as outlined by Crutcher et al. (2004). In units of μG , this can be expressed as:

$$B_{\text{pos}} = 9.3 \sqrt{n_{\text{H}_2}} \Delta V / \delta \phi, \quad (3)$$

where n_{H_2} is the number density in cm^{-3} , ΔV is the molecular linewidth from an optically thin species in km s^{-1} , and $\delta \phi$ is the dispersion in the magnetic field lines in degrees. Even though the DCF method has been revisited over time to explore its limitations and applicability (see reviews by Liu et al. 2021; Myers et al. 2024), we aimed to mitigate biases in this work by simplifying our analysis and minimizing assumptions. Consequently, we employed the “standard” DCF method, incorporating only the 1/2 correction proposed by numerical simulations (see Crutcher et al. 2004, for a comprehensive discussion). We will explore the implication of this in Section 4.2.2.

Our objective here is to derive a map with estimations of the magnetic field strength onto the plane of the sky (see Figure 9). To do that, we employ the number density model map, the velocity dispersion, ΔV , obtained from the $C^{33}S$ moment-two map (see Figure 10), and a position angle dispersion map, $\delta \phi$. We use the $C^{33}S$ emission because it is optically thin (see Section 3.4.2), and thus it provides a good account of the nonthermal motions of the warm and dense gas. Although as we inspected the data cube only a single component of the line was observed, it is difficult to rule out, or remove, the small outflow contribution to the $C^{33}S$ emission. Nonetheless and because the emission is compact with a very small deviation from the model at the line wings (see Section 3.4.2), we assume that this contamination is minimal. Although it does not overlap completely with the polarized dust emission, the $C^{33}S$ emission has sufficient coverage around the most relevant cores in NGC6334I to provide a good account of turbulence in this region.

The dispersion in the magnetic field lines is obtained by taking the standard deviation over a moving window of $1''.5$ in

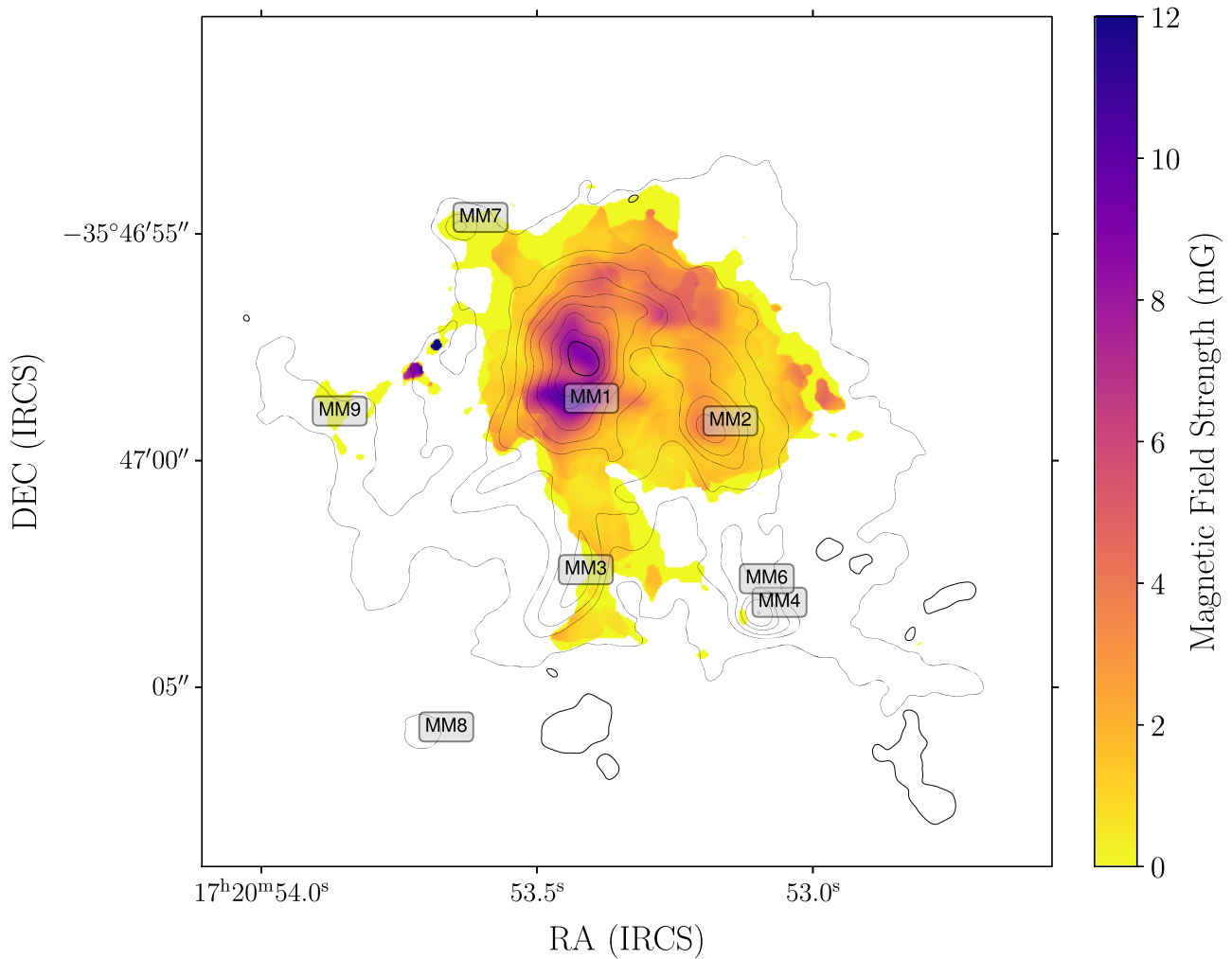


Figure 9. The figure shows the estimated field strength map onto the plane of sky determined by using the DCF method over a moving window of $1''.5$ used to estimate the position angle dispersion by means of circular statistics. Superposed to the map we add the dust continuum emission as contours following Figure 1 and the source labels as previously shown in Figure 1.

size. This kernel is $\sim 4 \times$ the beam size, which gives us about 16 independent points per window to calculate the standard deviation using circular statistics under the assumption of a 5° error in the polarization position angle (see Appendix B for a discussion about the statistics of the moving window). The window size used here has sufficient statistical significance to produce a believable estimate for the angular dispersion but also encloses the local fluctuations in the field, which are seen to occur in angular scales of $\sim 1''$ by visual inspection. While our goal is to account for the best possible estimate of the magnetic-field-line local dispersion, we also strive to prevent skewing our results in areas where the magnetic field appears uniform. To achieve this, we are cautious about selecting a larger moving window size, which could inadvertently include areas exhibiting significant fluctuations in the magnetic field's direction (i.e., regions where the field shows $\sim 90^\circ$ turns). Therefore, a value of $1''.5$ in size for the moving window appears to be a good compromise to achieve these objectives (Appendix B offers a more detailed discussion showing the effect of increasing the moving window size). Note that it is entirely plausible that the sudden turns in 90° are due to projection effects and not because of perturbation in the field lines. If that were to be the case, the estimated dispersion from those regions would be artificially large, which would decrease

the estimated field strength and thus the values around those regions should be considered as lower bounds for the magnetic field strength onto the plane of the sky. Thus, under these considerations, the B_{pos} map estimate is shown in Figure 9. The mean magnetic field strength estimated value is ~ 1.9 mG with a peak of ~ 11 mG toward the MM1 protocluster. Note that a strong outlier to the east of MM1 appears to be the result of small statistics at that point, which we ignore. Although Li et al. (2015) estimated $B_{\text{pos}} = 12$ mG at scales of 0.1 pc from the SMA data, our mean value is lower, which can be explained because of the coarser SMA resolution that smooths the field morphology and also because of their distance assumption to NGC6334 (1.7 kpc), which yields an overestimation of the mean density. Our estimate is consistent with the magnetic field strengths reported in a more recent analysis of the SMA data by Palau et al. (2021).

4.2.1. A Total Magnetic Field Estimation

Additional insight can be obtained from the results obtained by Hunter et al. (2018), who measured the magnetic field on the line of sight, B_{los} , by detecting the Zeeman effect from OH maser emission yielding magnetic field strengths between $+0.5$ and $+3.7$ mG toward the CM2 source and -2 to -5 mG

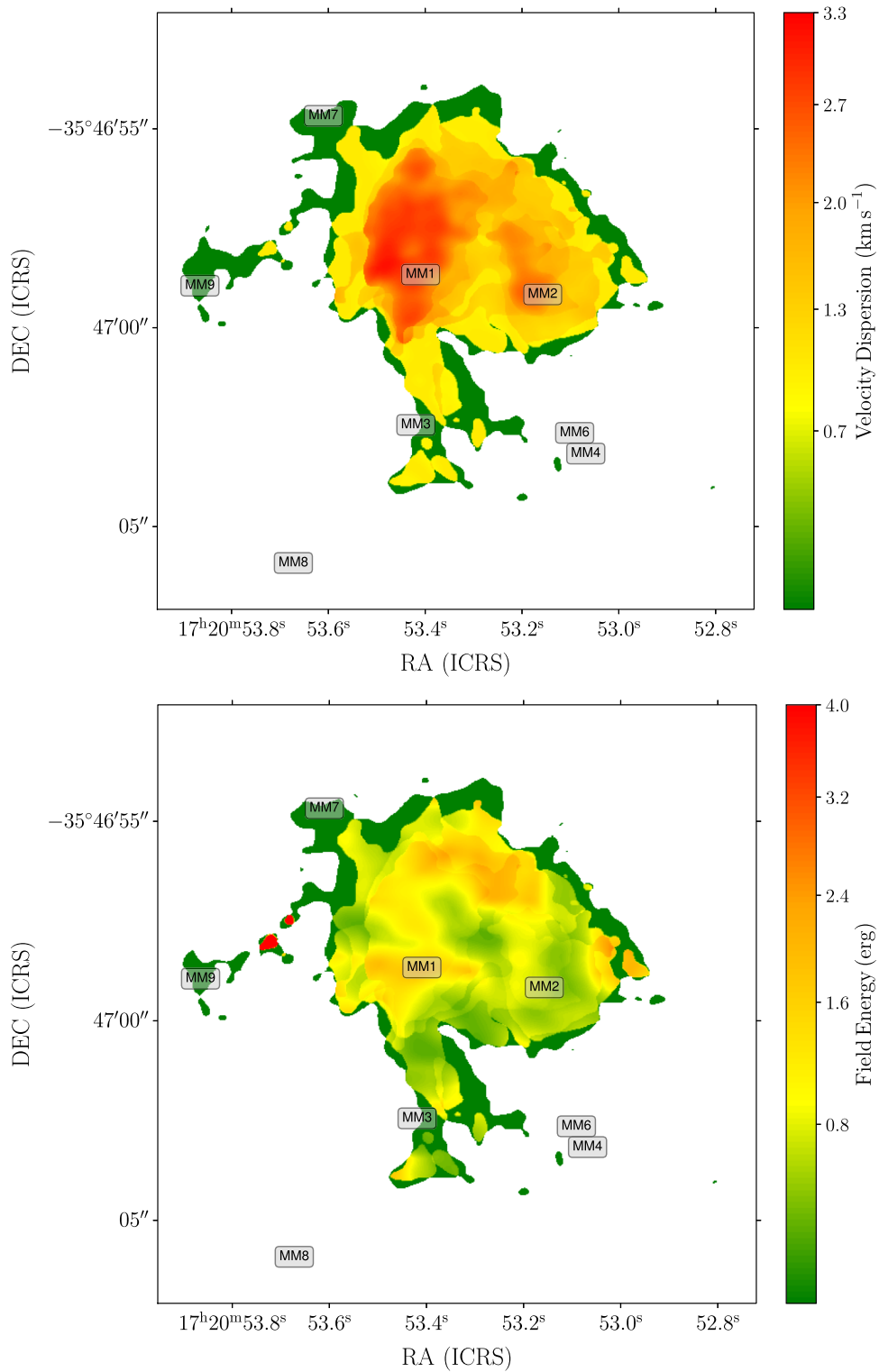


Figure 10. Upper panel: The moment-two map from the C³³S emission from NGC6634I is presented here. The color scale indicates the velocity dispersion in km s⁻¹ where no correction from the mean velocity field has been applied. Lower panel: The Alfvén speed map, as a color scale, is calculated from the magnetic field strength onto the plane of the sky, and our number density model is presented here.

around the MM3 H II region. Although their resolution, ~ 520 au, appears to be larger than the likely physical size of a maser spot, their measurements appear consistent with others (Caswell et al. 2011). We find our field estimates onto the plane of the sky, B_{pos} , consistent with this range in field strength. The OH maser emission detected by Hunter et al. (2018) is

associated with regions within our map (CM2 and MM3) and with gas at densities between 10^5 and 10^8 cm⁻³ according to the models of Cragg et al. (2002), which are within the ranges covered by our density model. This allows us to estimate the total magnetic strength field by computing the vector sum $B = \sqrt{B_{\text{pos}}^2 + B_{\text{los}}^2}$. Hunter et al. (2018) found the distribution

of OH masers to be well correlated with methanol masers at 6.7 GHz and with the MM3 UC H II region and CM2 source. However, there seems to be a consistent lack of maser emission toward the strongest continuum peaks in NGC6334I, particularly the MM1 protocluster where 80% of the maser emission is found outside the 40% level of the continuum in their ALMA 1 mm data. This suggests that the density in the strongest dust emission peaks in MM1 is too high to support inversion (Hunter et al. 2018). Thus, to add the OH Zeeman measurement to our magnetic field map, we decided to take the average of the absolute values from Hunter et al. (2018) Table 8, or $\langle B_{\text{los}} \rangle = 3.4$ mG, and compute the vector sum with the average of our B_{pos} values. This yields a total magnetic field estimate $\mathcal{B} = 4$ mG. In principle, one would have liked to add the Zeeman values following a density profile. However, the coverage of the maser emission is sparse and we lack a well-defined canonical shape of the field which might have allowed us to produce a total magnetic field map. This \mathcal{B} estimate is consistent with extrapolations derived by assuming a field strength dependency with density as obtained from CN Zeeman measurements (Crutcher & Kemball 2019) and by estimations using the DCF method, and its variants, toward other high mass star forming regions (HMSFR) (Beltrán et al. 2019; Cortés et al. 2021b; Sanhueza et al. 2021).

4.2.2. Caveats

The DCF technique has a number of caveats which have been explored in a number of works (Heitsch et al. 2001; Crutcher et al. 2004; Falceta-Goncalves et al. 2008; Cho & Yoo 2016; Cortes et al. 2019; Liu et al. 2021; Skalidis & Tassis 2021; Lazarian et al. 2022; Myers et al. 2024). Here, we mention the most important caveats that might be affecting the validity of our analysis in order to give perspective to the conclusions that we are deriving here. The DCF technique provides an estimate of the field strength onto the plane of the sky by assuming equipartition between turbulence and magnetic energy without considering self-gravitation and the anisotropic nature of turbulence. A region such as NGC6334I has already formed a number of protostars suggesting that the gas is far from an equilibrium situation. Although the effect of self-gravity in the dispersion of the position angle is difficult to quantify, gravity manifests itself over long distances requiring large reservoirs of mass to have a significant effect. Thus, the injection of turbulence by gravity into the gas, which will ultimately perturb the field, might happen at larger scales than the one traced by our moving box. Another issue relates to the velocity dispersion obtained from the C^{33}S moment-two map, which contains contributions from the mean velocity field which in this region might come from the outflow, infalling motions, and (or) rotation, in addition to turbulence. These components cannot be immediately removed because we lack sufficient information about the kinematics and geometry of the source. In short, we might be overestimating the nonthermal motions due to turbulence, which will bias the estimation of the field strength as well as the sonic Mach number (see Section 4.4 for a discussion).

The estimation of the density model is also subjected to a number of assumptions that are almost impossible to quantify. For instance, the determination of the column density map in our data is not only affected by flux calibration and temperature model uncertainties, but also by line-of-sight contamination, field selection, and most importantly by interferometric spatial

filtering (see Ossenkopf-Okada et al. 2016). Because we constructed the density model assuming a temperature model which may be overestimating the actual dust temperature, the B_{pos} values might be underestimations. In the case of the dispersion in the field lines, the proxy used here is the dispersion in the linear polarization angle of the ALMA polarized dust emission. Although we are subtracting the estimated error from the data in quadrature and using circular statistics, the true local perturbations to the mean magnetic field lines might be smoothed out by projection effects, such as tangling of the field along the line of sight, the different number of turbulent cells in the line of sight, beam smearing (though the beam obtained sampling our observations traces scales of 0.002 pc close to the dissipation length scale proposed by Li et al. 2010, of 0.001 pc), and others, which might produce overestimations of B_{pos} .

Despite the fact that these caveats are difficult to quantify, we will attempt to produce an error estimate for B_{pos} . We do this by simple propagation of errors over Equation (3) and by considering error estimates of the physical parameters that we can quantify (see Appendix C for a detailed derivation). The error estimates that we obtained are $\sigma_n = 5 \times 10^7 \text{ cm}^{-3}$ for the number density, $\sigma_v = 2 \text{ km s}^{-1}$ for the velocity dispersion, and $\sigma_{\delta\phi} = 5^\circ$ for the position angle dispersion. Using these values, we obtain a mean B_{pos} error estimate, $\langle \sigma_B \rangle = 1$ mG after rounding, which yields $\langle B_{\text{pos}} \rangle = 1.9 \pm 1$ mG. From the values of B_{los} obtained by Hunter et al. (2018), we estimate an error also of 1 mG which after adding them in quadrature and rounding we obtained $\langle \mathcal{B} \rangle = 4 \pm 1$ mG.

Finally, we should put in perspective that despite these caveats and simple error estimation, our estimates are consistent with values derived toward other HMSFR which are in line with what we should expect from extrapolations of the Zeeman effect to the densities traced by our data. Finally, in the absence of the Zeeman effect, the DCF technique is the simplest method that we have to obtain an estimate of field strength in star-forming regions and thus the values derived here should be considered as such.²⁵

4.3. Energy Balance

To understand the effects of the multiple physical parameters on the magnetic field, we calculate energy maps associated with turbulence (kinetic energy), gravitational, thermal, and magnetic. The kinetic energy map is estimated by computing

$$K = \frac{1}{2} \int \rho v^2 d^3x, \quad (4)$$

which for every pixel in the map can be approximated by

$$K_{i,j} = \frac{1}{2} m_{i,j} \Delta v_{i,j}^2, \quad (5)$$

where $m_{i,j}$ is the mass per pixel obtained from the column density map, $\Delta v_{i,j}$ is the velocity dispersion obtained from the C^{33}S moment-two map where we remove the contribution from the thermal sound speed. The dispersion is calculated as $\Delta v_{i,j} = \sqrt{\Delta v_{\text{obs},i,j}^2 - \sigma_{\text{th}}^2}$, where $\Delta v_{\text{obs},i,j}$ is the observed velocity dispersion per pixel from the C^{33}S moment-two map, and $\sigma_{\text{th}} = \sqrt{k_B T_{i,j}} / m_{\mu\text{H}_2}$ is the sound speed determined

²⁵ The intensity gradient technique is an alternative method that we will consider in subsequent work (see Koch et al. 2012a, 2012b, 2013).

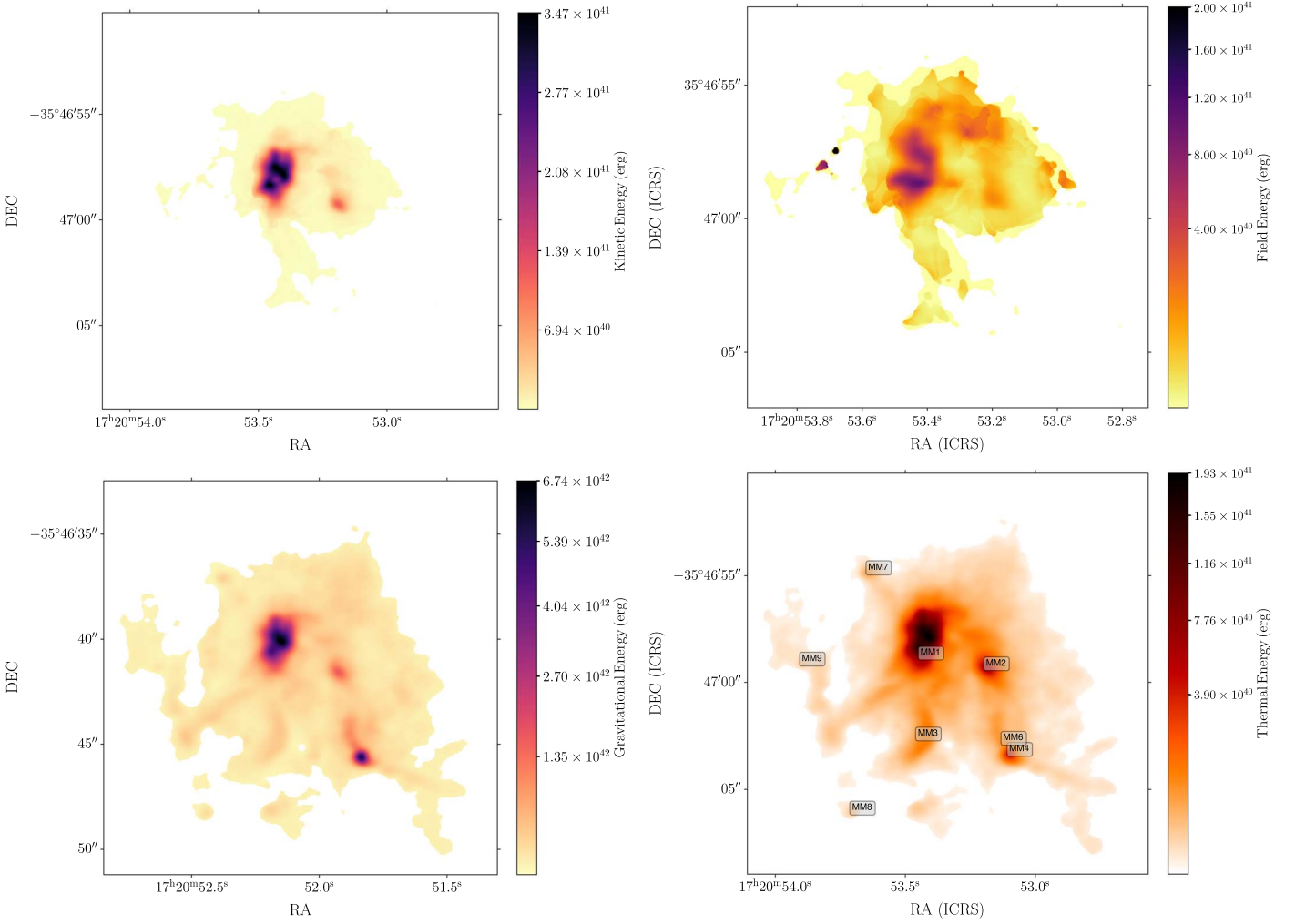


Figure 11. Upper panel: The kinetic and magnetic energy maps are shown here. The extent of the maps is given by the $C^{33}S$ moment-two map which is smaller than the extent of the dust continuum (see Figure 6). Lower panel: The magnetic field and thermal energy maps are shown here. Their extension is given by the dust continuum map that was used to define the temperature model (see Section 3.2). The source labels are shown over the thermal energy map only to improve visual inspection.

from the temperature model (see Figure 11), where k_B is the Boltzmann constant. The gravitational energy is calculated as

$$W = \frac{1}{2} \int \rho \Phi_g d^3x, \quad (6)$$

where Φ_g is gravitational potential. This expression can also be approximated by

$$W_{ij} = \frac{1}{2} m_{ij} \sum_{k,l} \left(-G \frac{m_{k,l}}{|r_{ij} - r_{k,l}|} \right), \quad (7)$$

where the indices (i,j) and (l,k) indicate pixel positions in the map, m_{ij} is the mass at pixel (i,j) , $|r_{ij} - r_{k,l}|$ is the distance between the mass elements at pixels (i,j) and (l,k) obtained from the column density map. Although the gravitational energy is negative, we plot the absolute value in Figure 11. Note that the underlying assumption here is that the dust emission is optically thin. If the dust emission is optically thick toward the more massive cores, the estimated gravitational energy will be a lower bound. The thermal energy can be expressed as

$$U = \frac{3}{2} \int nk_B T d^3x, \quad (8)$$

where we assume an ideal gas equation of state. As done before, the thermal energy per pixel can be expressed as

$$U_{ij} = \frac{3}{2} k_B n_{ij} T_{ij} \delta V_{ij}, \quad (9)$$

where n_{ij} is the number density per pixel, T_{ij} is the model temperature per pixel, and δV_{ij} is the pixel volume. We calculate the pixel volume as follows, given $m_{ij} = \rho_{ij} V_{ij} = \mu_{H_2} m_{H_2} n_{ij} V_{ij}$ and using $m_{ij} = \mu_{H_2} m_{H_2} A n_{ij}$, the pixel volume can be written as $V_{ij} = A n_{ij} / n_{ij}$, where $A \sim 1000 \text{ au}^2$ is the pixel area.²⁶ This yields the thermal energy per pixel as

$$U_{ij} = \frac{3}{2} A k_B n_{ij} T_{ij}. \quad (10)$$

The magnetic field energy density per pixel is calculated as

$$M = \frac{1}{8\pi} \int B^2 d^3x. \quad (11)$$

²⁶ A square circumscribing each beam has 256 pixels.

Table 5
Energy Balance

Region	Kinetic 10^{46} (erg)	Thermal Gas 10^{46} (erg)	Thermal H II 10^{46} (erg)	Gravitational 10^{46} (erg)	Outflow 10^{46} (erg)	Magnetic 10^{46} (erg)	Balance 10^{46} (erg)
MM1	0.147	0.025	...	0.762	...	0.016	-0.918
MM2	0.214	0.040	...	1.3	...	0.037	-1.485
MM4	0.013	0.002	...	0.070	...	0.002	-0.082
NGC6334I	0.538	0.100	0.14	3.163	0.350	0.087	-3.714

Note. The energies are calculated by summing all the pixels inside the region and balance is calculated by subtracting all the energies from the magnetic field energy. The region labeled NGC6334I corresponds to the whole total intensity map. The energy in the expanding cometary UC H II region and the outflows are considered only for the bulk of NGC6334I.

Following the thermal energy calculation, the magnetic field energy per pixel can be estimated as

$$M_{i,j} = \frac{A}{8\pi} B_{i,j}^2 N_{i,j} / n_{i,j}, \quad (12)$$

where $B_{i,j}$ is the magnetic field strength onto the plane of sky estimated using the DCF method, $N_{i,j}$ is the column density per pixel, and $n_{i,j}$ is the number density per pixel (also see Figure 11).

We also estimate the energy coming from the expanding MM3 cometary H II region by assuming that the emission is purely free-free, which we use to estimate its thermal energy. Sadaghiani et al. (2020) obtained continuum emission with ALMA at 87.6 GHz. From these data, we estimate the size of the MM3 cometary H II by a Gaussian fit to their data, which gives us a region of $3''.3 \times 2''.5$ in size. The electron temperature, $T_e = 10^4$ K, and density, $n_e = 3 \times 10^6 \text{ cm}^{-3}$ are taken from Brogan et al. (2016) simple free-free model. Thus using these values and assuming the geometrical thickness used for our density model, we obtain $\mathcal{E}_{\text{H II}} \sim 10^{45}$ [erg].

The energy balance against the magnetic field is calculated by subtracting the turbulent, thermal (both gas and UC H II), and gravitational energies from the magnetic field energy as

$$\Delta E = M - (U + W + K + \mathcal{E}_{\text{H II}} + \mathcal{E}_{\text{outflow}}), \quad (13)$$

where $\mathcal{E}_{\text{outflow}}$ corresponds to the combined energy in the red and blue lobes of the outflows. The results of the energy balance are listed in Table 5. We do not compute values for MM7 and MM9 because we do not have sufficient C^{33}S coverage over these cores to obtain the velocity dispersion. From these results, it is clear that there is sufficient energy in the system to perturb the magnetic field in NGC6334I, even when considering the large uncertainties introduced by our assumptions. The differences in energy are about 2 orders of magnitude between the field and the combined effects of the other forces around the main cores and in the whole of NGC6334I. The gravitational energy is clearly the dominant factor in the energetics of the region, which is expected given its evolutionary stage. Nonetheless, the energy in the outflows alone is an order of magnitude larger than the magnetic energy and because the outflows might be injecting turbulence at smaller scales than gravity, the outflow feedback might be a significant factor when considering the perturbation to the magnetic field morphology. Interestingly, the energy in the cometary UC H II region, a single UC H II region, is comparable to the bulk of the thermal energy over the whole of NGC6334I. Thus, the expansion of this UC H II region might also inject additional turbulence in the gas at similar scales to those of the outflows. Thus, protostellar feedback may be the

dominant driver behind the injection of turbulence in NGC6334I at the scales sampled by our data. Finally, the analysis done here suggests that a magnetic field on the order of mG appears not to be a dominant factor at the core scales in NGC6334I.

4.4. Effect of the Field in the Dynamics of the Gas

To study the effect of the magnetic field on the gas dynamics, one can start by comparing the different speeds relevant to the physical processes affecting the gas. These are the sound speed, the nonthermal velocity dispersion, obtained from optically thin molecular emission, and the Alfvén speed, which we compute from estimates of the magnetic field strength. Both the velocity dispersion and the Alfvén speed can be used as proxies for the different modes of hydromagnetic waves, which encompass what we understand as MHD turbulence (Mouschovias et al. 2011). Although complex in nature, in principle we can compare thermal to kinetic by computing the Mach number, or \mathcal{M}_s , and kinetic to magnetic by computing the Alfvén Mach number, or \mathcal{M}_A . For supersonic motions, nonthermal motions dominate the dynamics where thermal energy only becomes relevant at larger densities. However, if the magnetic field is strong enough, we can have a sub-Alfvénic regime, where $\mathcal{M}_A < 1$ and $\rho V^2 \leq B^2$, which is still supersonic. In this case, the magnetic field can significantly influence the dynamics through the Lorentz force (Beattie et al. 2020). In the super-Alfvénic regime where $\mathcal{M}_A > 1$, the magnetic field plays a lesser role, but different hydromagnetic wave modes still exist which can influence the gas dynamics (Mouschovias et al. 2011).

Preliminary studies done with the SMA, Herschel, and APEX over the whole of the NGC6334 molecular cloud complex, suggested that ($\mathcal{M}_s \sim 6$), but sub-Alfvénic ($\mathcal{M}_A \sim 0.9$) at resolutions of ~ 0.2 pc (Zernickel 2015). Furthermore, Li et al. (2015) estimated the magnetic field onto the plane of the sky to conclude that the gas motions in NGC6334 are also likely to be sub-Alfvénic. Recently, ALMA observations of the NGC6334S IRDC (also part of the NGC6334 complex) used emission from H^{13}CO^+ and NH_2D , to explore the nonthermal motions in the IRDC at 0.02 pc resolution with ALMA (Li et al. 2020). They found that the spatially unresolved nonthermal motions are predominantly subsonic and transonic ($\sim 77\%$ regions), but they made no estimations about the Alfvénic regime of the filament. The sub-to-transonic-dominated regime in the NGC6334S IRDC suggests that the region is at a very early evolutionary stage such that the protostellar feedback-induced turbulence is small as compared to the initial turbulence (Li et al. 2020). These findings were confirmed by Liu et al. (2023a) who explored the

evolution of the sonic Mach number from large scales (~ 15 pc resolution) to small scales (~ 0.005 pc resolution) finding the gas is mostly supersonic over 3–4 orders of magnitude in length-scales over most of NGC6334, but subsonic to transonic in NGC6334S (the IRDC), which is consistent with what has already been observed in other IRDCs (Sanhueza et al. 2017). This IRDC is at an earlier stage of evolution with respect to NGC6334I, but because is part of the same molecular complex, the cores in NGC6334S may indicate what were the initial conditions in NGC6334I.

We investigate the nonthermal motions in NGC6334I to explore how much influence the magnetic field has in the gas dynamics. To achieve this, we compute the sound speed map using the temperature model map, represented as $c_s = \sqrt{k_B T / m_H}$. Employing the velocity dispersion map derived from $C^{33}S$ (see Section 4.3), we estimate the sonic Mach number map using $\mathcal{M}_s = \sqrt{3} c_s / \Delta V$ (see Figure 12). The Mach number map suggests that the gas is supersonic throughout most of the regions covered by the $C^{33}S$ emission in NGC6334I. Mach number values as high as $\mathcal{M}_s \sim 4$ suggest that nonthermal motions are high with turbulence being injected at the core scales to sustain the gas velocity dispersion seen here. Our values for the sonic Mach number are consistent with the previous results and with a number of other evolved high-mass star-forming regions (Pattle et al. 2023; Pineda et al. 2023). To estimate the Alfvénic regime, we calculate the Alfvén speed $V_A = \mathcal{B} / \sqrt{4\pi\rho}$ but using B_{pos} as an estimate of \mathcal{B} . The V_A corresponds to the propagation speed of the transverse waves along the magnetic field lines. These motions do not involve compressions or rarefactions of the gas, meaning there is no density variation associated with these waves (different from the fast and slow magnetosonic modes). Interestingly, when using solely B_{pos} as the \mathcal{B} estimate, the Alfvén speed does not depend on the density. This is because $V_A = B_{\text{pos}} / \sqrt{4\pi\rho} = \delta V / \delta\phi$ when introducing the original DCF equation, $B_{\text{pos}} = \sqrt{4\pi\rho} \delta v / \delta\phi$, into the Alfvén speed expression. Because DCF assumed equipartition over the total magnetic field, a derivation of the Alfvén speed based on the DCF alone is as good as the B_{pos} estimate and subjected to the same caveats. We show the Alfvén speed map in Figure 10. Estimates of the Alfvén speed from the literature are scarce. However, Roshi (2007) estimated Alfvén speeds ranging between 0.7 and 4 km s $^{-1}$ based on carbon recombination line observations conducted with the Arecibo telescope. These observations targeted a set of 14 PDRs surrounding H II regions associated with high-mass star-forming regions. Liu et al. (2020) estimated Alfvén speeds from their polarization mapping of the G28.34 + 0.06 IRDC, finding values between 0.5 and 1.5 km s $^{-1}$. The values from both studies are consistent with our findings (see Figure 10).

From the Alfvén speed map alone it is difficult to explore the effect of the field in the gas. To this effect, we can compute the Alfvén Mach number map using $\mathcal{M}_A = \Delta V / V_A$ (also see Figure 12). As with the Alfvén speed, we note that the Alfvén Mach number depends only on the dispersion of the magnetic field lines when assuming DCF, which gives $\mathcal{M}_A \sim \delta\phi$. We found this approach convenient because, in principle, it allows for an estimate of this quantitative from the polarization map alone. Furthermore, the Alfvén Mach number map derived here is not affected by the assumptions used to derive the temperature and density models. Furthermore, even by considering different variants of DCF, the Alfvén Mach

number will still strongly depend on the dispersion of the magnetic field lines. The Alfvén Mach number map shown in Figure 12, strongly suggests that most of NGC6334I appears to be in trans-Alfvénic conditions ($\mathcal{M}_A \sim 1$) evolving to super-Alfvénic conditions ($\mathcal{M}_A > 1$) as we move into the cores. Although there are regions at the edges of the map that may be sub-Alfvénic ($\mathcal{M}_A < 1$), their extension is small and thus inconclusive given the area covered by the $C^{33}S$ mask. In trans-Alfvénic conditions, the nonthermal motions can be considered to be in equipartition with the magnetic field, suggesting that the effect of the magnetic field and MHD turbulence are comparable. As density increases due to the gravitational pull, the Alfvén Mach number becomes super-Alfvénic where the magnetic field is dominated by nonthermal motions. This becomes evident over the peaks with $\mathcal{M}_A \sim 4$, where the exception is MM4 where the $C^{33}S$ emission is marginal (see Figure 6). These results agree well with the study by Pattle et al. (2023) who found that the turbulence is mostly trans-Alfvénic when statistics are compiled over many sources. The strongest peaks in the Alfvén Mach number map also correlate well with the regions where we see $\sim 90^\circ$ deviations in the field orientation within scales of 1". Note, if the region were sudden $\sim 90^\circ$ turns are the product of projection effects, then the estimated dispersion in the field should decrease the dispersion in the field lines increasing the estimated value for B_{pos} at those regions. Conversely, this should also decrease the value of \mathcal{M}_A in those regions as well. The transition seen from trans-Alfvénic to super-Alfvénic in NGC6334I is consistent with an evolved HMSFR such as NGC6334I where gravity dominates the gas dynamics and the magnetic field appears to be dynamically important only at the edges of the region. Interestingly, new high angular resolution ($\sim 0''.065$) ALMA results from the ‘‘hourglass’’ magnetic field in G31.41 + 0.31 suggests that the gas can evolve from sub-Alfvénic to super-Alfvénic in a progression resembling NGC6334I, if we were to assume that the edges of our Alfvénic Mach number map correspond to a sub-Alfvénic regime (Beltrán et al. 2024). Now, when considering the whole NGC6334 molecular complex, exploring the Alfvénic state on NGC6334I(N), a source supposedly in an earlier stage of evolution, might show a more conclusive sub-Alfvénic to super/trans-Alfvénic condition from the outer to inner regions of the clump while the NGC6334S IRDC might likely be sub-Alfvénic. This would certainly give us significant insight into the evolutionary effect of the magnetic field over the gas dynamics in NGC6334. We leave this for future work.

5. Summary and Conclusions

We have presented subarcsecond-resolution results from polarized dust emission and total intensity line emission observations, at 250 GHz, toward NGC6334I with ALMA. The results can be summarized as follows:

1. The morphology of the magnetic field onto the plane of the sky was derived from 1.2 mm polarized dust emission under the assumption of grain alignment by magnetic fields. The magnetic field morphology is in close agreement with the ALMA results from Liu et al. (2023) taken at 1.4 mm.
2. Our two-epoch data over five months show no substantial change in total intensity ($< 1\%$) or linear polarization

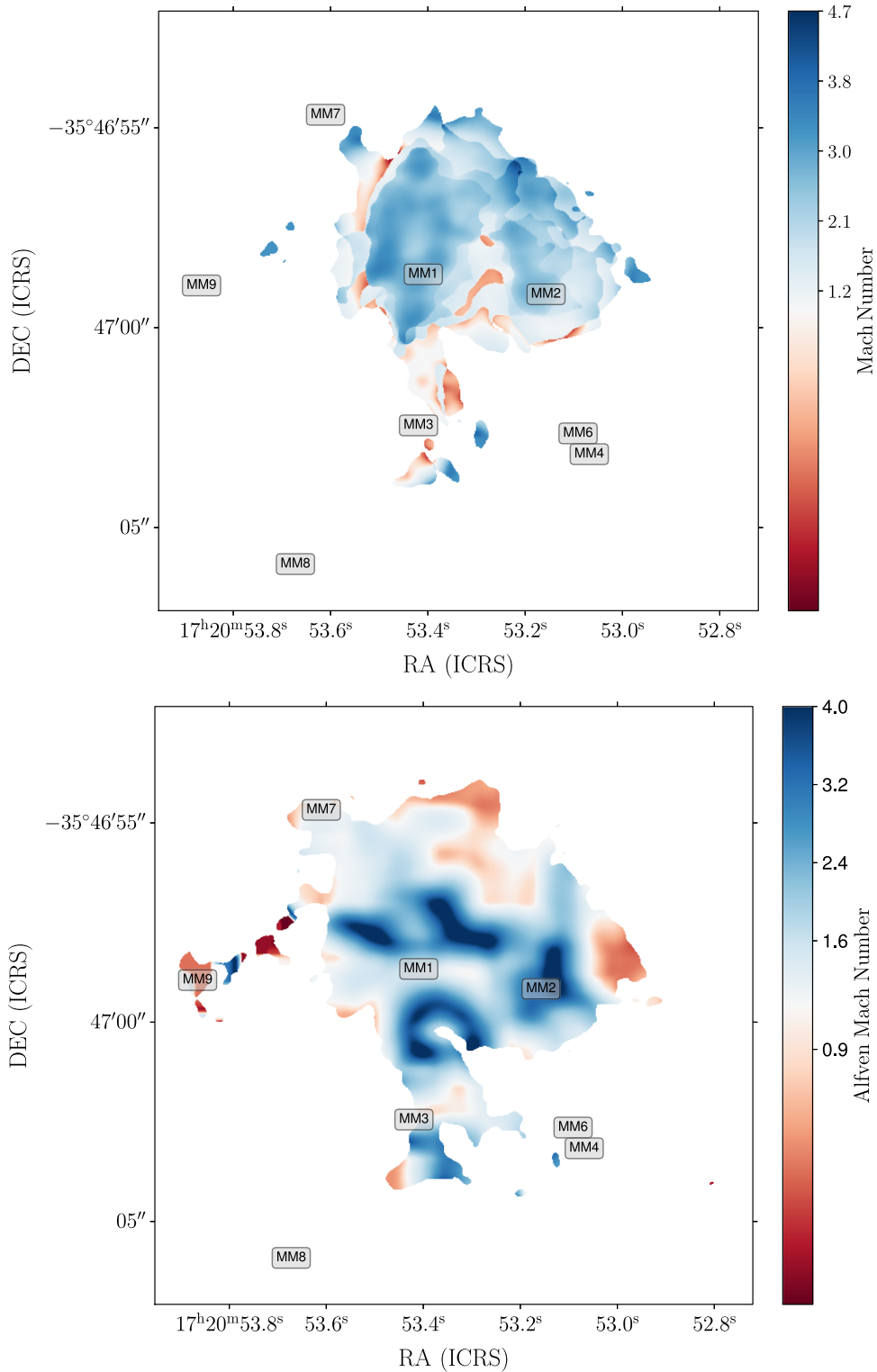


Figure 12. Upper panel: The sonic Mach number map, \mathcal{M}_s , is shown in color scale. Lower panel: The Alfvén Mach number map, \mathcal{M}_A , is also shown in color scale where trans-Alfvénic conditions are represented by color values ~ 1 .

- ($< 8\%$), indicating a stable period or the end of the outburst.
- 3. To explore the effect of the four outflows detected from NGC6334I in the magnetic field, we quantified their energy by making use of the CS emission. We found that the bulk energy in the outflows is $\sim 3.5 \times 10^{45}$ erg.

- 4. By making use of the temperature model produced by Liu et al. (2023), we computed energy maps for the kinetic, thermal, gravitational, and magnetic fields, whose strength onto the plane of the was estimated using the DCF technique obtaining values between 1 and 11 mG with a mean magnetic field strength of 1.9 mG. When we

add Zeeman measurements from OH maser observations (Hunter et al. 2018), we estimate a mean total magnetic field strength of 4 ± 1 mG in agreement with others.

5. While the magnetic field in NGC6334I holds considerable energy, our analysis reveals that the cumulative effect of kinetic, thermal, and gravitational energies, alongside the contributions from outflows and the external pressure exerted by the surrounding cometary H II region, is capable of overpowering the magnetic field. Furthermore, the energy from the outflows alone may sufficiently disturb the field lines through the injection of turbulence at the core scales. At the same time, gravity-induced turbulence is likely to occur on larger scales. Therefore, protostellar feedback potentially emerges as the primary influence on the observed perturbations in the magnetic field's structure across NGC6334I.
6. By making use of the optically thin $C^{33}S$ emission, we computed a velocity dispersion map which we use as a proxy for the nonthermal motions. Also, by using the temperature map, we computed the thermal sound speed map and the sonic Mach number map. We found that the gas is mostly supersonic throughout NGC6334I consistent with previous findings. In the same way, we estimated the Alfvén speed, which we used to compute the Alfvén Mach number. From the Alfvén Mach number map, we found indications suggesting that gas smoothly evolves from trans-Alfvénic to super-Alfvénic, with possibly sub-Alfvénic regions when we consider the outer edges of the map. This suggests that we may be seeing the progression at which the field finally gets overwhelmed by the effects of protostellar feedback-induced turbulence and gravity in high-mass star formation.

Acknowledgments

P.C.C. acknowledges publication and travel support from ALMA and NRAO. P.S. was partially supported by a Grant-in-Aid for Scientific Research (KAKENHI No. JP22H01271 and JP23H01221) of JSPS. J.M.G. acknowledges support by the grant PID2020-117710GB-I00 (MCI-AEI-FEDER, UE). This work was also supported by the NAOJ Research Coordination Committee, NINS (NAOJ-RCC-2202-0401). This work is also partially supported by the program Unidad de Excelencia María de Maeztu CEX2020-001058-M. L.A.Z acknowledges financial support from CONACyT-280775 and UNAM-PAPIITIN110618 grants, Mexico. A.S.-M. acknowledges support from the RyC2021-032892-I grant funded by MCIN/AEI/10.13039/501100011033 and by the European Union 'Next GenerationEU'/PRTR, as well as the program Unidad de Excelencia María de Maeztu CEX2020-001058-M, and support from the PID2020-117710GB-I00 (MCI-AEI-FEDER, UE). This work was supported by the NAOJ Research Coordination Committee, NINS (NAOJ-RCC-2202-0401). This paper makes use of the following ALMA data: ADS/JAO.

ALMA#2018.1.00105.S. ALMA is a partnership of ESO (representing its member states), NSF (USA), and NINS (Japan), together with NRC (Canada), MOST and ASIAA (Taiwan), and KASI (Republic of Korea), in cooperation with the Republic of Chile. The Joint ALMA Observatory is operated by ESO, AUI/NRAO, and NAOJ. The National Radio Astronomy Observatory is a facility of the National Science Foundation operated under a cooperative agreement by Associated Universities, Inc.

Facility: ALMA

Software: CASA (CASA Team et al. 2022). Astropy (Astropy Collaboration et al. 2018). MADCUBA (Martín et al. 2019).

Appendix A

Comparison with Lower Frequency Polarization Results

As previously mentioned, the magnetic field morphology in NGC6334I at comparable resolutions but lower frequencies, has already been explored with ALMA (Liu et al. 2023). Here we compare our results to those of Liu et al. (2023), where we see significant consistency between the field morphology obtained at 250 GHz (our data) with respect to the results from 220 GHz (Liu et al. 2023). Figure 13 shows the superposed field morphologies obtained independently by both data sets. Our data set was re-gridded to the frame and resolution of the 220 GHz data ($0''.67 \times 0''.52$) to allow for a direct comparison. When inspecting Figure 13, it is clear that the field morphologies are remarkably similar over most of the extent of the Stokes I emission. The most significant deviation between both data sets is seen at the center of the MMI protocluster. The 250 GHz data shows an N–S orientation while the 220 GHz data presents a more east–west orientation. This difference in the field morphology is significant ($\Delta\phi \sim 35^\circ$, see Figure 14) when compared to the rest of the map where the pseudovectors agree quite well. To explore if this is the result of calibration uncertainties, Figure 15 shows the derived magnetic field morphology at both frequencies, but now the pseudovectors are colored to indicate the level of fractional polarization (the fractional polarization maps have 3σ cutoff in Stokes I and a coarser sampling rate). At the center, where the Stokes I peaks and the difference in angle is the largest, the range of fractional polarization is between 0.1% and 0.15% in both data sets. Although this range is close to the polarization calibration accuracy of ALMA (0.1% Cortés et al. 2023), it is sufficiently large to suggest that the difference might be real. Given the current data sets, it is difficult to ascertain what is the cause of such differences, particularly considering the excellent overall agreement between them throughout the region where both data sets are separated by just 30 GHz. Polarized emission by self-scattering appears implausible as an explanation (as discussed in Section 3.3). High-resolution ALMA observations in full Stokes should be conducted to explore this discrepancy further.

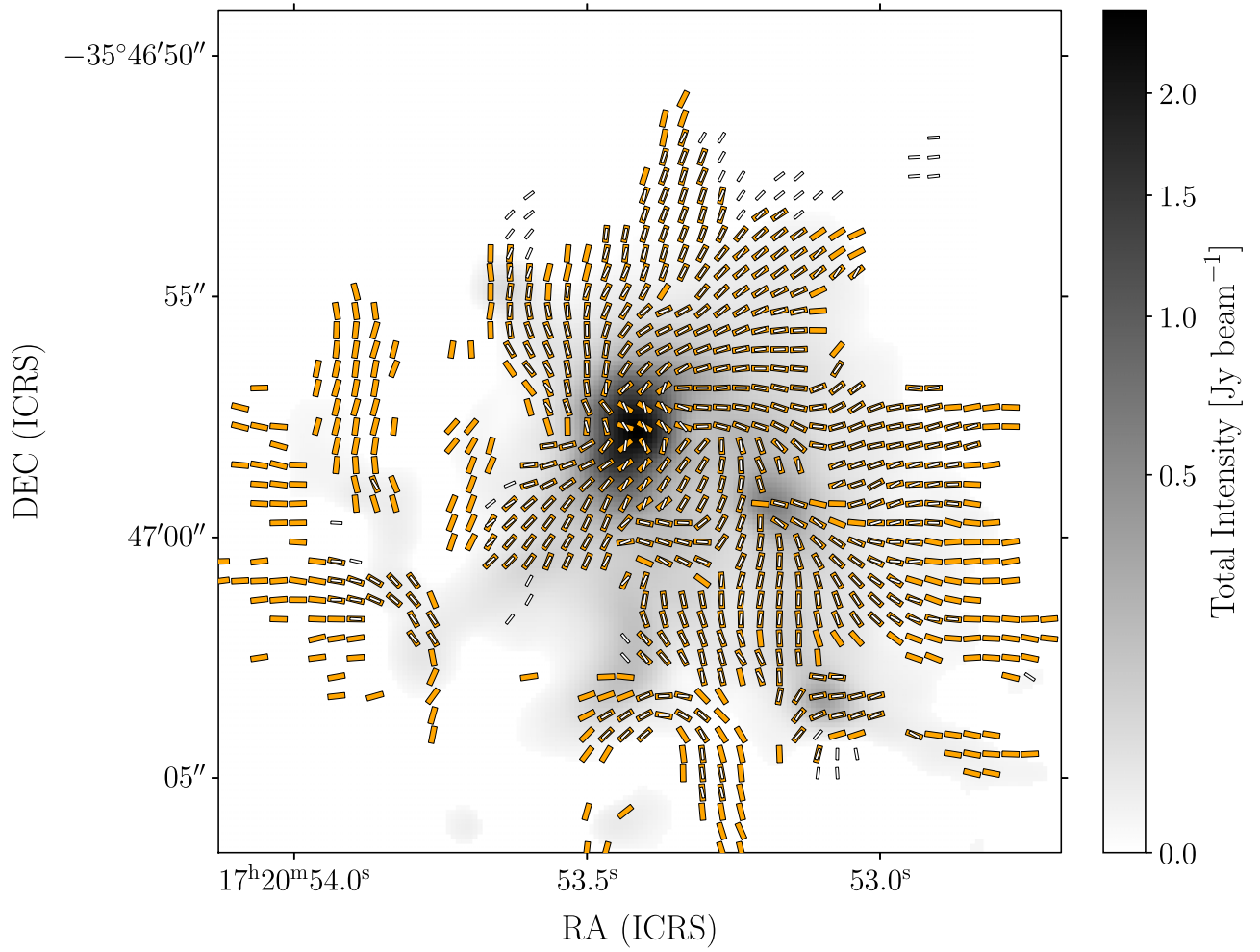


Figure 13. Magnetic field morphology in NGC6334I derived from polarized dust emission at 220 GHz (white pseudovectors) and 250 GHz (orange pseudovectors). The gray scale corresponds to the Stokes I from 250 GHz dust emission. The white pseudovectors were plotted using a smaller length and width to allow comparison between the two different field morphologies.

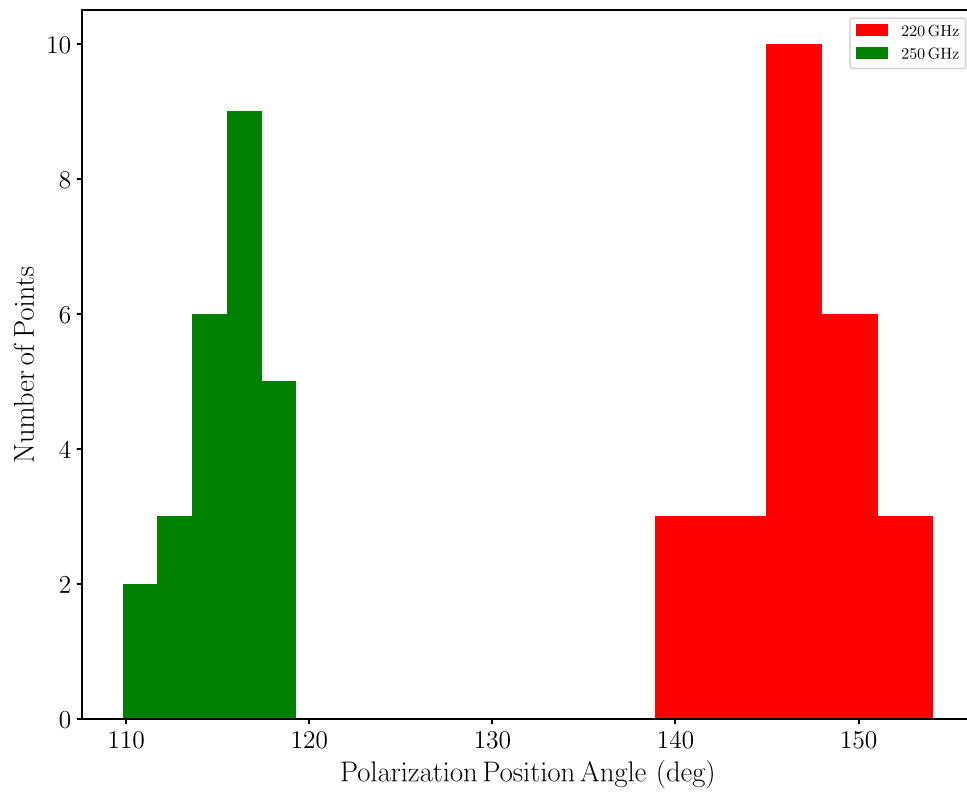


Figure 14. The histogram shows the position angle values between 220 GHz (Liu et al. 2023) and 250 GHz (ours). A clear separation of $\sim 35^\circ$ is seen from the histogram.

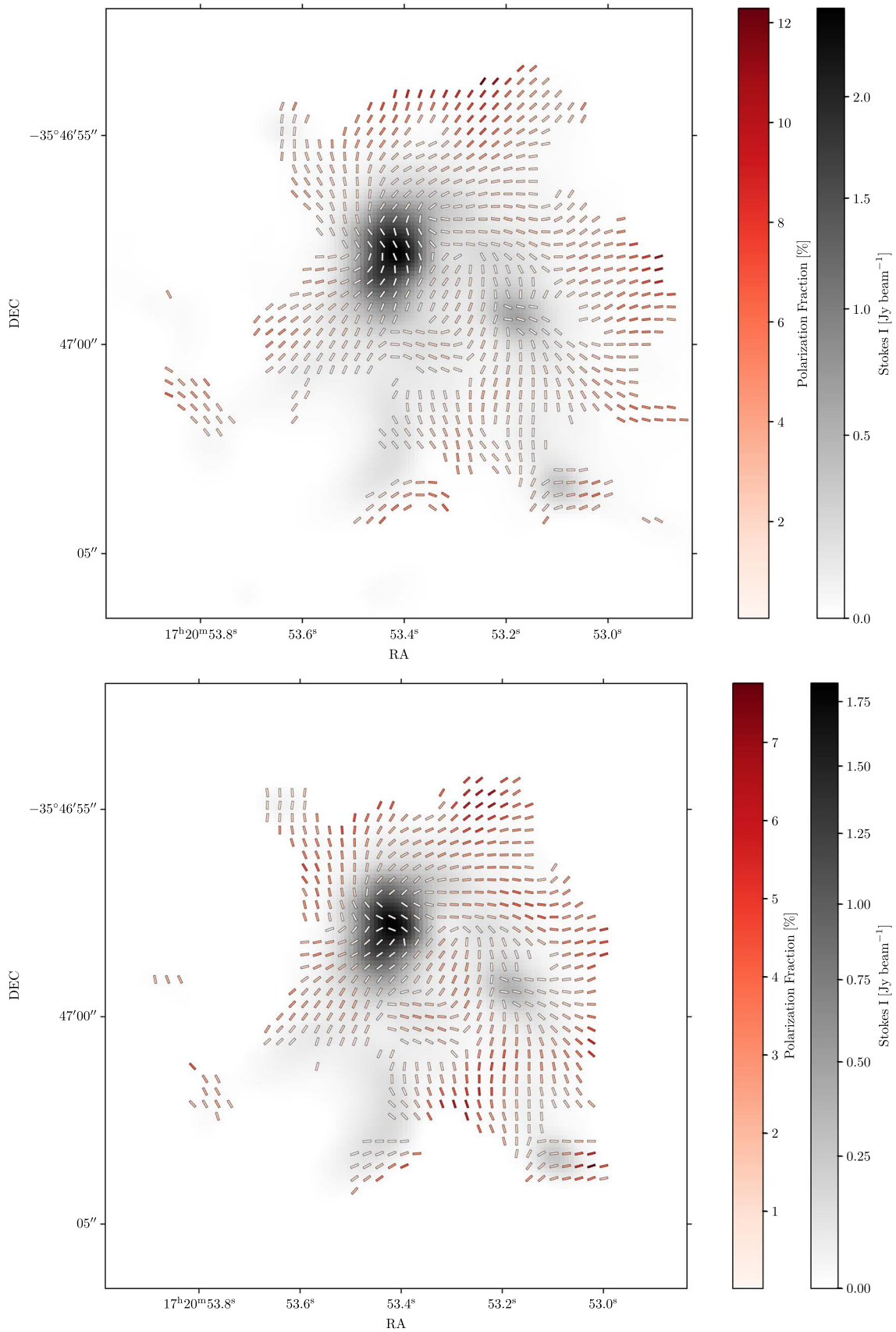


Figure 15. The magnetic field morphology maps are shown here for both 220 GHz (upper panel) and 250 GHz (lower panel). The color scale was used in the pseudovectors and indicates fractional polarization values while the gray scale indicates Stokes I (total intensity) emission.

Appendix B The Magnetic Field Dispersion Map

To estimate the magnetic field strength onto the plane of the sky using DCF, estimating the dispersion in the polarization position angle is critical. Because we assume flux freezing, the local dispersion in the field lines is produced by collisions between the charge carriers and the neutrals. These collisions perturb the mean field yielding deviations in its local direction, which we understand as the dispersion. The dispersion is a statistical quantity and thus we will use statistical arguments to estimate its value. Because we are interested in obtaining a map, we make use of a moving window to calculate the standard deviation using semicircular statistics. To define the size of the window, we assume that the angles follow a Gaussian distribution. Although Gaussian distribution is a “usual” assumption in astronomy, its usage here can be justified from the point of view of the central limit theorem. If we assume that the perturbations over the field lines are local then each independent point in the map can be considered as a random variable following its own distribution due to the actions of the local turbulence. In the limit of large numbers, the distribution of the mean of all independent points follows a Gaussian distribution. Moreover, local turbulence can also be modeled using a Gaussian distribution as done by Houde et al. (2009) in their angle dispersion function approximation which

also provides an alternative method to derive the dispersion in the field. Therefore and under this consideration, we use the standard error of the mean as:

$$SE = \frac{\sigma}{\sqrt{N}}, \quad (\text{B1})$$

where σ is the population standard deviation (unknown but can be estimated from the sample), and N is the population size. For a 95% confidence interval (which might be akin to a 95% credible interval in a Bayesian context, although the interpretation is different), the margin of error is

$$ME = 1.96 \times SE. \quad (\text{B2})$$

If we assume a margin of error to be within 5° , then $1.96 \times s/\sqrt{N} = 5$ gives the number of independent points required for an error of 5° , where s is the estimate of σ . To estimate s , we take the mean of the standard deviation over regions in the map where the field appears to be coherent, by visual inspection, on scales of $\sim 1''$. This gives us an initial population standard deviation estimate of $s \sim 10^\circ$. Thus, we obtain $N=16$ independent points as the required number (beams), which when assuming Nyquist sampling for the beam, we obtain a window of $1''.5$ in size. The final dispersion map is

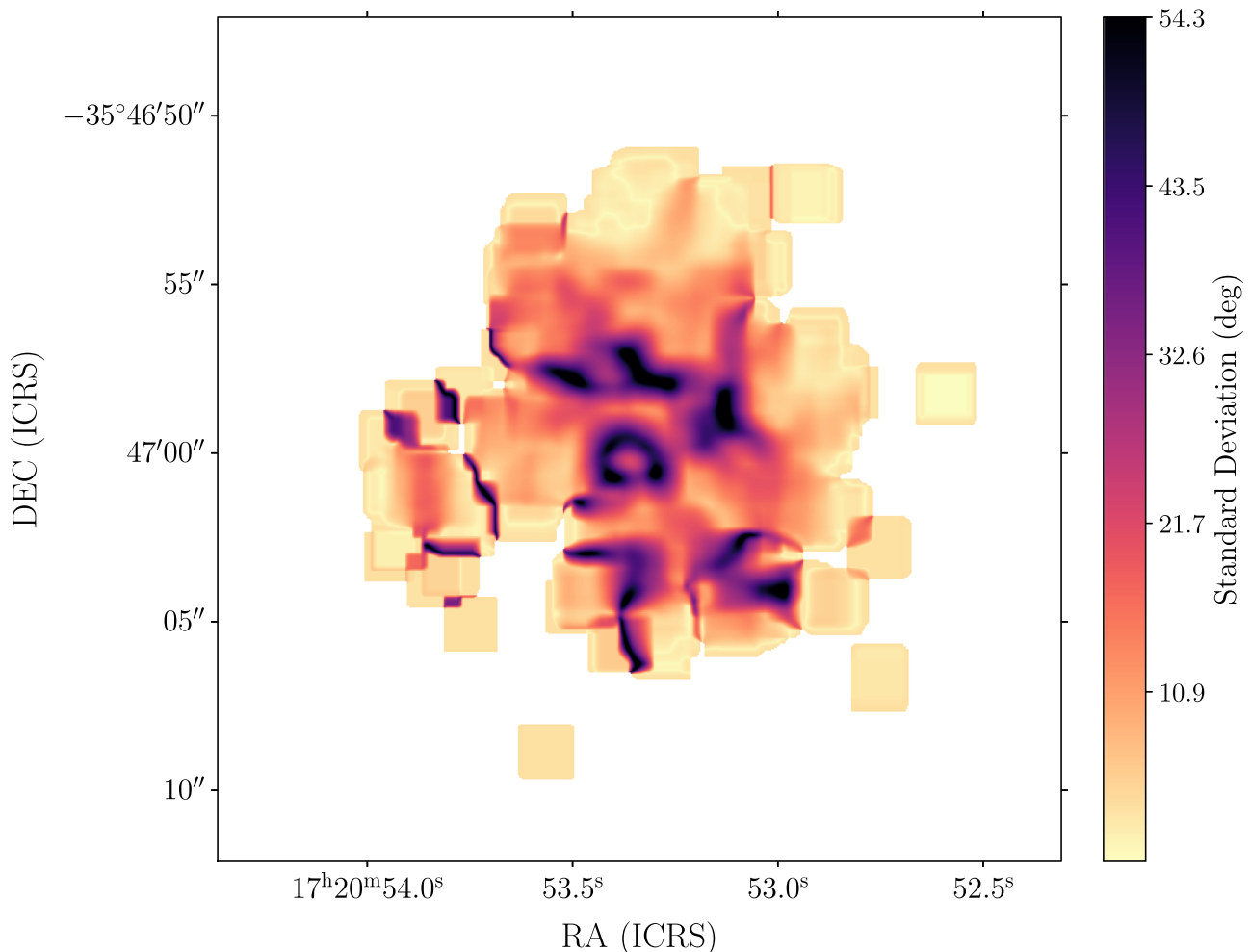


Figure 16. The position angle dispersion map from NGC6334I computed using a moving window of $1''.5$ is shown here. The values for the standard deviation are shown in color scale.

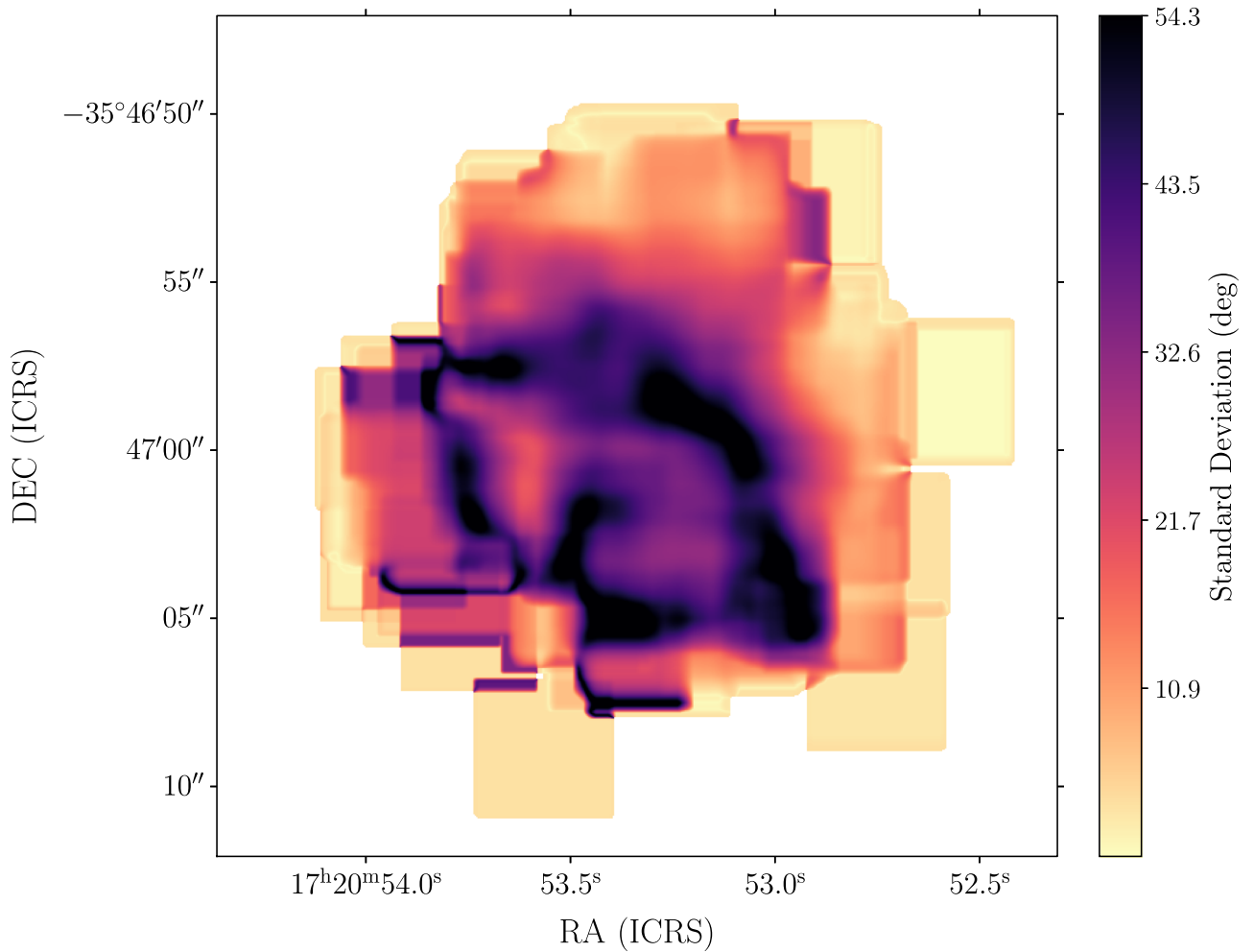


Figure 17. The position angle dispersion map from NGC6334I computed using a moving window of $4''$ is shown here. The values for the standard deviation are shown in color scale.

Table 6
Position Angle Dispersion Error Estimate

Window Size (arcsec)	Number of Beams	Dispersion Error (deg)
1.0	6	8
1.5	16	5
2.0	25	4
2.5	40	3
3.0	56	3
4.0	100	2
5.0	156	2
6.0	225	1
7.0	306	1

Note. The errors were rounded to a single integer for consistency and the number of beams assumed Nyquist sampling.

calculated as:

$$\delta\phi_{i,j} = \sqrt{\sigma_{i,j}^2 - \sigma_{err,i,j}^2}, \quad (\text{B3})$$

where $\sigma_{err,i,j} = \sigma P / 2P_{i,j}$ represents the error in the polarization position angle in an ALMA map, with σP and P being the rms and the polarization intensity respectively (Hull et al. 2020).

Although the choice of $5''$ may appear arbitrary, we found it to be a good compromise (see Figure 16). A smaller window results in a larger error, while a larger window not only smooths out the map but also biases regions where the field appears smooth. This is because it propagates larger deviations in the field lines seen in the regions where the field has 90° turns; regions where DCF is likely not fully applicable. An example of this can be seen in Figure 17 where we show a dispersion map using a window of $4''$. This window size has an estimated error of $\sim 2^\circ$, but the spatial distribution of dispersions values over 25° is significantly larger than our current choice (see Figure 16). Analysis of the DCF technique done by comparing with simulations suggests that the applicability of DCF decreases with dispersion values over 25° (see Crutcher et al. 2004, and references therein). Table 6 shows the error estimates for the position angle dispersion for window sizes ranging from $1''$ to $7''$.

Finally, it is important to note that the maximum value for the standard deviation under semicircular statistics is $\sim 54.45^\circ$. This is because, the maximum dispersion is achieved when we have a uniform distribution over the semicircle with a probability density function of $p(r) = 1/\pi$, which yields $\sigma = \sqrt{-2 \log 2/\pi}$.

Appendix C

Simple Error Estimation for DCF

Although a number of caveats constrain the interpretation of our result from DCF (see Section 4.2.2), here we attempt to quantify these uncertainties by employing simple error propagation to estimate an uncertainty value for B_{pos} . The expression that we used for DCF is given by Equation (3), which under simple error propagation becomes,











$$\delta B_{\text{pos}} = 3 \sqrt{\left(\frac{n^{-3/2} \Delta V}{\delta \phi} \sigma_n\right)^2 + \left(\frac{\sqrt{n}}{\delta \phi} \sigma_{\Delta V}\right)^2 + \left(\frac{\sqrt{n} \Delta V}{\delta \phi^2} \sigma_{\delta \phi}\right)^2}, \quad (\text{C1})$$








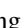
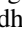


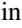
where σ_n , $\sigma_{\Delta V}$, and $\sigma_{\delta \phi}$ are the uncertainties in the number density, velocity dispersion, and position angle dispersion respectively. The most difficult quantity to estimate is the number density error, because of the uncertainties previously mentioned. We attempt to circumvent this by calculating the mean absolute error between our model and the values derived by Brogan et al. (2016). Because both data sets come from ALMA observations from the same source, a number of systematics can be removed by taking the difference between their values and our model. In this way, the mean absolute error can be calculated as,

$$\sigma_n = \frac{\sum_i^N |n_{i,1} - n_{i,2}|}{N}, \quad (\text{C2})$$

where $n_{i,1}$ corresponds to the number density estimate done by Brogan et al. (2016) on source i , $n_{i,2}$ is the number density estimate from our model over source i , and N is the total number of sources. In this way, we obtained $\sigma_n = 5 \times 10^7 \text{ cm}^{-3}$ as the number density error. The uncertainty in the velocity dispersion is estimated by the resolution used in the spectral setup of the C^{33}S line, or $\sigma_{\Delta V} = 2 \text{ km s}^{-1}$, while the error estimate for the position angle dispersion is $\sigma_{\delta \phi} = 5^\circ$ (see Appendix B also for a discussion about the impact a different windows sizes in the error estimate). With all of these values, we obtain a mean B_{pos} error estimate, $\langle \sigma_B \rangle = 1 \text{ mG}$ after rounding, which yields $\langle B_{\text{pos}} \rangle = 1.9 \pm 1 \text{ mG}$. From the values of B_{pos} obtained by Hunter et al. (2018), we estimate an error also of 1 mG which after adding them in quadrature and rounding we obtained $\langle B \rangle = 4 \pm 1 \text{ mG}$.

ORCID iDs

Paulo C. Cortés  <https://orcid.org/0000-0002-3583-780X>
 Josep M. Girart  <https://orcid.org/0000-0002-3829-5591>
 Patricio Sanhueza  <https://orcid.org/0000-0002-7125-7685>
 Junhao Liu  <https://orcid.org/0000-0002-4774-2998>
 Sergio Martín  <https://orcid.org/0000-0001-9281-2919>
 Ian W. Stephens  <https://orcid.org/0000-0003-3017-4418>
 Henrik Beuther  <https://orcid.org/0000-0002-1700-090X>
 Patrick M. Koch  <https://orcid.org/0000-0003-2777-5861>
 M. Fernández-López  <https://orcid.org/0000-0001-5811-0454>
 Álvaro Sánchez-Monge  <https://orcid.org/0000-0002-3078-9482>
 Jia-Wei Wang  <https://orcid.org/0000-0002-6668-974X>
 Kaho Morii  <https://orcid.org/0000-0002-6752-6061>
 Shanghuo Li  <https://orcid.org/0000-0003-1275-5251>
 Piyali Saha  <https://orcid.org/0000-0002-0028-1354>

Qizhou Zhang  <https://orcid.org/0000-0003-2384-6589>
 David Rebolledo  <https://orcid.org/0000-0002-1010-583X>
 Luis A. Zapata  <https://orcid.org/0000-0003-2343-7937>
 Ji-hyun Kang  <https://orcid.org/0000-0001-7379-6263>
 Wenyu Jiao  <https://orcid.org/0000-0001-9822-7817>
 Jongsoo Kim  <https://orcid.org/0000-0002-1229-0426>
 Yu Cheng  <https://orcid.org/0000-0002-8691-4588>
 Jihye Hwang  <https://orcid.org/0000-0001-7866-2686>
 Eun Jung Chung  <https://orcid.org/0000-0003-0014-1527>
 Spandan Choudhury  <https://orcid.org/0000-0002-7497-2713>
 A-Ran Lyo  <https://orcid.org/0000-0002-9907-8427>
 Fernando Olguin  <https://orcid.org/0000-0002-8250-6827>

References

- Arzoumanian, D., André, P., Didelon, P., et al. 2011, *A&A*, 529, L6
 Arzoumanian, D., Furuya, R. S., Hasegawa, T., et al. 2021, *A&A*, 647, A78
 Astropy Collaboration, Price-Whelan, A. M., Sipőcz, B. M., et al. 2018, *AJ*, 156, 123
 Bachiller, R., & Cernicharo, J. 1990, *A&A*, 239, 276
 Beattie, J. R., Federrath, C., & Seta, A. 2020, *MNRAS*, 498, 1593
 Beltrán, M. T., Padovani, M., Galli, D., et al. 2024, *A&A*, 686, A281
 Beltrán, M. T., Padovani, M., Girart, J. M., et al. 2019, *A&A*, 630, A54
 Beuther, H., Gieser, C., Soler, J. D., et al. 2024, *A&A*, 682, A81
 Beuther, H., Soler, J. D., Linz, H., et al. 2020, *ApJ*, 904, 168
 Beuther, H., Walsh, A. J., Thorwirth, S., et al. 2008, *A&A*, 481, 169
 Brogan, C. L., Hunter, T. R., Cyganowski, C. J., et al. 2016, *ApJ*, 832, 187
 Brogan, C. L., Hunter, T. R., Cyganowski, C. J., et al. 2018, *ApJ*, 866, 87
 Burns, R. A., Uno, Y., Sakai, N., et al. 2023, *NatAs*, 7, 557
 Bustreel, R., Demuyneck-Marlière, D., Destombes, J., & Journel, G. 1979, *CPL*, 67, 178
 CASA Team, Bean, B., Bhatnagar, S., et al. 2022, *PASP*, 134, 114501
 Caswell, J. L., Kramer, B. H., & Reynolds, J. E. 2011, *MNRAS*, 414, 1914
 Chandrasekhar, S., & Fermi, E. 1953, *ApJ*, 118, 113
 Chibueze, J. O., Omodaka, T., Handa, T., et al. 2014, *ApJ*, 784, 114
 Cho, J., & Yoo, H. 2016, *ApJ*, 821, 21
 Ciolek, G. E., & Mouschovias, T. C. 1994, *ApJ*, 425, 142
 Cortes, P., Vlahakis, C., Hales, A., et al. 2023, ALMA Cycle 10 Technical Handbook, Version Cycle 10; Doc. 10.3; v1.1, Zenodo, doi:10.5281/zenodo.7822943
 Cortes, P. C., Crutcher, R. M., & Watson, W. D. 2005, *ApJ*, 628, 780
 Cortes, P. C., Girart, J. M., Hull, C. L. H., et al. 2016, *ApJL*, 825, L15
 Cortes, P. C., Hull, C. L. H., Girart, J. M., et al. 2019, *ApJ*, 884, 48
 Cortes, P. C., Le Gouellec, V. J. M., Hull, C. L. H., et al. 2021a, *ApJ*, 907, 94
 Cortés, P. C., Sanhueza, P., Houde, M., et al. 2021b, *ApJ*, 923, 204
 Cragg, D. M., Sobolev, A. M., & Godfrey, P. D. 2002, *MNRAS*, 331, 521
 Crutcher, R. M., & Kemball, A. J. 2019, *FrASS*, 6, 66
 Crutcher, R. M., Nutter, D. J., Ward-Thompson, D., & Kirk, J. M. 2004, *ApJ*, 600, 279
 Davis, L. 1951, *Phys. Rev.*, 81, 890
 Falceta-Gonçalves, D., Lazarian, A., & Kowal, G. 2008, *ApJ*, 679, 537
 Feddersen, J. R., Arce, H. G., Kong, S., et al. 2020, *ApJ*, 896, 11
 Fernández-López, M., Sanhueza, P., Zapata, L. A., et al. 2021, *ApJ*, 913, 29
 Girart, J. M., Frau, P., Zhang, Q., et al. 2013, *ApJ*, 772, 69
 Girart, J. M., Rao, R., & Marrone, D. P. 2006, *Sci*, 313, 812
 Heitsch, F., Zweibel, E. G., Mac Low, M.-M., Li, P., & Norman, M. L. 2001, *ApJ*, 561, 800
 Hildebrand, R. H. 1983, *QJRAS*, 24, 267
 Houde, M., Vaillancourt, J. E., Hildebrand, R. H., Chitsazzadeh, S., & Kirby, L. 2009, *ApJ*, 706, 1504
 Hull, C. L. H., Cortes, P. C., Gouellec, V. J. M. L., et al. 2020, *PASP*, 132, 094501
 Hull, C. L. H., Girart, J. M., Tychoniec, Ł., et al. 2017, *ApJ*, 847, 92
 Hull, C. L. H., & Plambeck, R. L. 2015, *JAI*, 4, 1550005
 Hull, C. L. H., Plambeck, R. L., Kwon, W., et al. 2014, *ApJS*, 213, 13
 Hunter, T. R., Brogan, C. L., Buizer, J. M. D., et al. 2021, *ApJL*, 912, L17
 Hunter, T. R., Brogan, C. L., Cyganowski, C. J., & Young, K. H. 2014, *ApJ*, 788, 187
 Hunter, T. R., Brogan, C. L., MacLeod, G., et al. 2017, *ApJL*, 837, L29
 Hunter, T. R., Brogan, C. L., MacLeod, G. C., et al. 2018, *ApJ*, 854, 170
 Kataoka, A., Tsukagoshi, T., Momose, M., et al. 2016, *ApJL*, 831, L12

- Koch, P. M., Tang, Y.-W., & Ho, P. T. P. 2012a, *ApJ*, 747, 79
- Koch, P. M., Tang, Y.-W., & Ho, P. T. P. 2012b, *ApJ*, 747, 80
- Koch, P. M., Tang, Y.-W., & Ho, P. T. P. 2013, *ApJ*, 775, 77
- Koch, P. M., Tang, Y.-W., Ho, P. T. P., et al. 2018, *ApJ*, 855, 39
- Koch, P. M., Tang, Y.-W., Ho, P. T. P., et al. 2022, *ApJ*, 940, 89
- Lazarian, A., & Hoang, T. 2007, *MNRAS*, 378, 910
- Lazarian, A., Yuen, K. H., & Pogosyan, D. 2022, *ApJ*, 935, 77
- Li, H., Li, D., Qian, L., et al. 2015, *ApJS*, 219, 20
- Li, H.-b., Houde, M., Lai, S.-p., & Sridharan, T. K. 2010, *ApJ*, 718, 905
- Li, S., Zhang, Q., Liu, H. B., et al. 2020, *ApJ*, 896, 110
- Liu, J., Zhang, Q., Commerçon, B., et al. 2021, *ApJ*, 919, 79
- Liu, J., Zhang, Q., Koch, P. M., et al. 2023, *ApJ*, 945, 160
- Liu, J., Zhang, Q., Koch, P. M., et al. 2023a, *ApJ*, 945, 160
- Liu, J., Zhang, Q., Liu, H. B., et al. 2023b, *ApJ*, 949, 30
- Liu, J., Zhang, Q., Qiu, K., et al. 2020, *ApJ*, 895, 142
- MacLeod, G. C., Smits, D. P., Goedhart, S., et al. 2018, *MNRAS*, 478, 1077
- Martín, S., Martín-Pintado, J., Blanco-Sánchez, C., et al. 2019, *A&A*, 631, A159
- McCutcheon, W. H., Sandell, G., Matthews, H. E., et al. 2000, *MNRAS*, 316, 152
- Mouschovias, T. C., Ciolek, G. E., & Morton, S. A. 2011, *MNRAS*, 415, 1751
- Myers, P. C., Stephens, I. W., & Coudé, S. 2024, *ApJ*, 962, 64
- Ossenkopf, V., & Henning, T. 1994, *A&A*, 291, 943
- Ossenkopf-Okada, V., Csengeri, T., Schneider, N., Federrath, C., & Klessen, R. S. 2016, *A&A*, 590, A104
- Palau, A., Zhang, Q., Girart, J. M., et al. 2021, *ApJ*, 912, 159
- Pattle, K., Fissel, L., Tahani, M., Liu, T., & Ntormousi, E. 2023, in ASP Conf. Ser. 534, Protostars and Planets VII, ed. S. Inutsuka et al. (San Francisco, CA: ASP), 193
- Pineda, J. E., Arzoumanian, D., Andre, P., et al. 2023, in ASP Conf. Ser. 534, Protostars and Planets VII, ed. S. Inutsuka et al. (San Francisco, CA: ASP), 233
- Rao, R., Crutcher, R. M., Plambeck, R. L., & Wright, M. C. H. 1998, *ApJL*, 502, L75
- Roshi, D. A. 2007, *ApJL*, 658, L41
- Sadaghiani, M., Sánchez-Monge, Á., Schilke, P., et al. 2020, *A&A*, 635, A2
- Sandell, G. 2000, *A&A*, 358, 242
- Sanhueza, P., Girart, J. M., Padovani, M., et al. 2021, *ApJL*, 915, L10
- Sanhueza, P., Jackson, J. M., Zhang, Q., et al. 2017, *ApJ*, 841, 97
- Savitzky, A., & Golay, M. J. E. 1964, *AnaCh*, 36, 1627
- Skalidis, R., & Tassis, K. 2021, *A&A*, 647, A186
- Tang, Y.-W., Ho, P. T. P., Girart, J. M., et al. 2009, *ApJ*, 695, 1399
- Tazaki, R., Lazarian, A., & Nomura, H. 2017, *ApJ*, 839, 56
- Wardle, J. F. C., & Kronberg, P. P. 1974, *ApJ*, 194, 249
- Yu, H. Z., Zhang, J. S., Henkel, C., et al. 2020, *ApJ*, 899, 145
- Zernickel, A. 2015, PhD thesis, Univ. of Cologne
- Zernickel, A., Schilke, P., Schmiedeke, A., et al. 2012, *A&A*, 546, A87
- Zhang, B., Moscadelli, L., Sato, M., et al. 2014a, *ApJ*, 781, 89
- Zhang, Q., Hunter, T. R., Brand, J., et al. 2001, *ApJL*, 552, L167
- Zhang, Q., Hunter, T. R., Brand, J., et al. 2005, *ApJ*, 625, 864
- Zhang, Q., Qiu, K., Girart, J. M., et al. 2014b, *ApJ*, 792, 116
- Zhang, Q., Qiu, K., Girart, J. M., et al. 2014c, *ApJ*, 792, 116
- Zhang, Y., Arce, H. G., Mardones, D., et al. 2016, *ApJ*, 832, 158